University of South Bohemia in České Budějovice

Faculty of Science

Numerical simulations of dynamic processes in the solar corona

Master's thesis

Bc. Sofya Belov

Supervisor: doc. RNDr. Petr Jelínek, Ph.D.

Consultant: Mgr. Miroslav Bárta, Ph.D.

České Budějovice 2022

Belov, S., 2022: Numerical simulations of dynamic processes in the solar corona. Mgr. Thesis, in English. – 54 p., Faculty of Science, University of South Bohemia, České Budějovice, Czech Republic.

Abstract

This master's thesis deals with 3D numerical simulations of turbulent flow past magnetic structures in the solar corona, focusing on the phenomenon of vortex shedding. This phenomenon is well known in hydrodynamic conditions. Still, it has not yet been satisfactorily investigated in magnetohydrodynamic (MHD) conditions, such as in the solar atmosphere, where its occurrence has been suggested by several studies and may explain some oscillatory phenomena. Numerical code Lare3d is used for the simulations.

Declaration

I declare that I am the author of this qualification thesis and that in writing it I have used the sources and literature displayed in the list of used sources only.

České Budějovice, April 13, 2022 .....

Sofya Belov

Acknowledgment

I would like to express my gratitude to my thesis supervisor, Assoc. Prof. Dr. Petr Jelínek, for valuable advice, support, motivation and all his time devoted to our consultations.

Contents

List of symbols

$\mathbf{v}$ ..... flow velocity

T ..... fluid tepmerature

ρ ..... fluid mass density

$\mathbf{B}$ ..... magnetic field

St ..... Strouhal number

P ..... vortex shedding period

r ..... cylinder radius

$\boldsymbol{\omega}$ ..... vorticity

m_p ..... proton mass

μ ..... average mass of particles in the plasma in the units of m_p

k_B ..... Boltzmann constant

μ_0 ..... vacuum permeability

γ ..... specific heat ratio

$\mathbf{g}_\odot$ ..... solar gravitational acceleration

1 Introduction

Solar physics is now one of the most dynamic astronomical branches. The understanding of the Sun has undergone a significant revolution in recent decades thanks to theoretical advances and observations. These include advances in analytical and computational methods and both terrestrial and space observations – see, for example, SoHO (Solar and Heliospheric Observatory), SDO (Solar Dynamics Observatory) [34], Parker Solar Probe [27] and Solar Orbiter [1].

Despite this progress, several important issues in solar physics have not yet been satisfactorily explained. For example, the physical processes heating the upper layers of the solar atmosphere have not been clearly identified. The Sun affects the Earth's climate and space weather [34], and due to its proximity to the Earth and its similarity to other stars, it plays an essential role in astrophysics [15]. Addressing these issues is therefore important both for a better ability to predict dangerous events in space weather and for gaining knowledge of other astrophysical systems [11].

This master's thesis is focused on dynamic processes in the solar corona, the outer layer of the solar atmosphere. This region is formed by an almost fully ionized plasma of a very high temperature [2], which is partly propagated into interplanetary space in the form of the solar wind but also kept in closed magnetic structures such as coronal loops [11].

The main task of the thesis is to perform a parametric study of turbulent processes taking place in the vicinity of these magnetic structures through numerical simulations, focusing on the phenomenon of vortex shedding. This phenomenon consists in the periodic formation of vortices during the flow around a cylindrical body (or another body causing high drag) [42] and will be described in more detail in a later chapter. The aim of this study is to determine the influence of the solar corona environment on the course and parameters of this phenomenon,

the occurrence of which is still lacking direct observational evidence in this environment. In hydrodynamics, the vortex shedding phenomenon is well known [35], but it has not yet been satisfactorily investigated in environments with a magnetic field [22], such as the solar corona, where it can explain some oscillating phenomena [29, 31, 35].

Numerical simulations of the vortex shedding phenomenon in two spatial dimensions have already been performed in bachelor thesis [8]. There, a hydrodynamic case in a gravity-free medium was investigated to determine the regularity of this phenomenon under different flow velocities and obstacle sizes and verify the model's functionality. One of the simulations was then repeated with the addition of a magnetic field perpendicular to the flow plane (using a so-called 2.5D model). In the current thesis, this model is extended to three dimensions and applied to the environment of the solar corona.

1.1 The solar corona

The solar corona is the highest layer of the solar atmosphere. It extends over the chromosphere at an altitude of about 2500 km above the visible surface of the Sun, or photosphere (see Fig. 1.1), to the interplanetary space [23] and consists of a sparse, almost fully ionized very high temperature plasma [2].

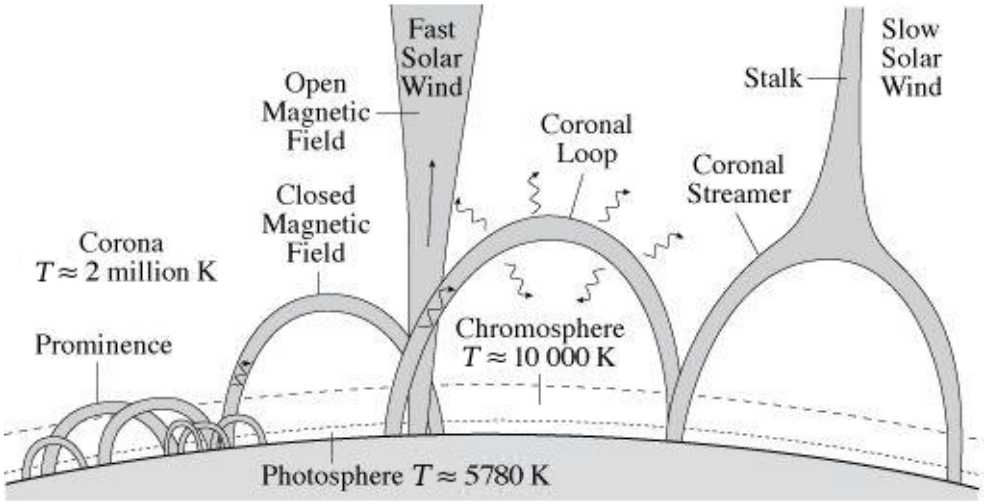

Figure 1.1: A scheme of the solar atmosphere and magnetic structures observed in it. Taken and edited from [28].

The scheme of the solar atmosphere with indicated structures, which will be mentioned below, is in Fig. 1.1. The temperature and density profile of the solar atmosphere according to the so-called C7 model [6] can be seen in Fig. 1.2, which shows that its temperature slowly increases at the chromosphere base and extremely rapidly increases from $\sim 10^4\,\mathrm{K}$ up to $\sim 10^6\,\mathrm{K}$ in the transition region between the chromosphere and corona. The coronal density in the lower region is of the order of $10^{-12}\ \mathrm{kg}\cdot\mathrm{m}^{-3}$ [23].

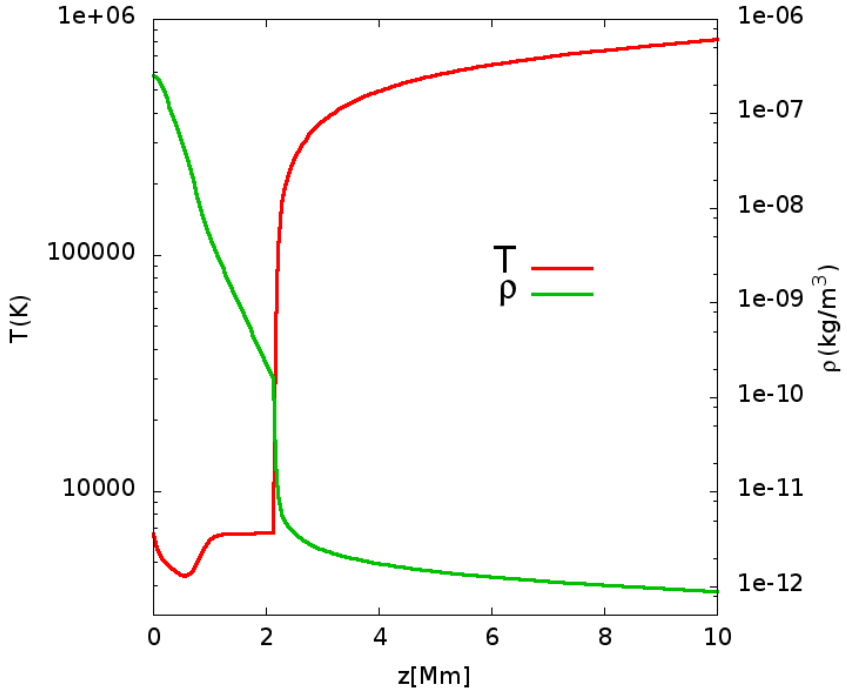

Figure 1.2: The temperature and density of the solar atmosphere as a function of height according to the so-called C7 model [6]. Taken from [19].

1.1.1 Magnetic structures

The movement of coronal plasma and particles that escape from the corona and form the solar wind is strongly influenced by the solar magnetic field. Its field lines directly determine the direction of this movement [37]. This magnetic field is highly variable, which is associated with the eleven-year cycle of solar activity during which the polarity of the Sun changes [30].

In the solar atmosphere, open field and closed field regions can be distinguished, as can be seen in Fig. 1.3. Open field regions are always located in the polar regions (depending on the period of solar activity, they can extend further) and reach up to interplanetary space. In closed

field regions, on the other hand, there are mostly closed magnetic field lines, reaching much smaller heights in the corona [37].

Coronal plasma can propagate freely into interplanetary space, or the heliosphere, only if the magnetic field lines reach this distance. In the case of the open field region, it is the so-called fast solar wind, which reaches speeds of $\sim 750\,\mathrm{km}\cdot\mathrm{s}^{-1}$ [30]. These field lines act as tubes into which plasma flows from the chromosphere and is carried into the interplanetary space as it passes through the corona [37].

Figure 1.3: An image of the Sun taken during the total solar eclipse in Chile in 2019, enabling to see the solar corona and the structure of the solar magnetic field. The open field regions, from where the coronal plasma propagates freely into inteplanetary space, and the close field regions, where the plasma density is increased due to the coronal loops, can be distiguished. In this image the Sun is close to the minimum phase of the solar activity cycle, when its magnetic field is most bipolar. Taken from [13].

In the closed field regions, structures called coronal loops are very abundant. They arise due to the flow of plasma from the chromosphere, which fills them and is kept in them due to closed magnetic field lines, which directly determine their shape [37]. Due to the densely contained plasma, they can radiate intensely at extreme ultraviolet and X-ray wavelengths [28]. In coronal loops with the bases further apart, the plasma density is lower [17]. Large loops form the basis for structures called coronal streamers, which reach into interplanetary space through an open structure called stalk and are the source of the so-called slow solar wind

[28], whose average speed is $\sim 350\,\mathrm{km}\cdot\mathrm{s}^{-1}$ [30]. Figure 1.4 shows an ultraviolet image of the solar surface capturing coronal loops.

Other magnetic structures that can be observed in the solar corona are prominences. They are formed by chromospheric matter protruding in the corona, which makes them on the order of a hundred times denser and cooler than the environment in which they are embedded [2]. Typically, they reach heights of 10–100 Mm and are composed of 15–20 threads with a 200–400 km width [5]. When observed above the solar limb, against the dark sky background, they take the form of bright clouds – see Fig. 1.5, while when observed on the solar disk, they appear as dark, thin and long features and are called filaments [2]. According to their dynamic nature, they can be divided into quiescent and eruptive prominences. Quiescent prominences are stable structures that last up to several months [5], probably supported against gravity by forces of magnetic origin [4, 7]. Eruptive prominences are usually associated with solar flares and coronal mass ejections (see Sec. 1.1.2) [5].

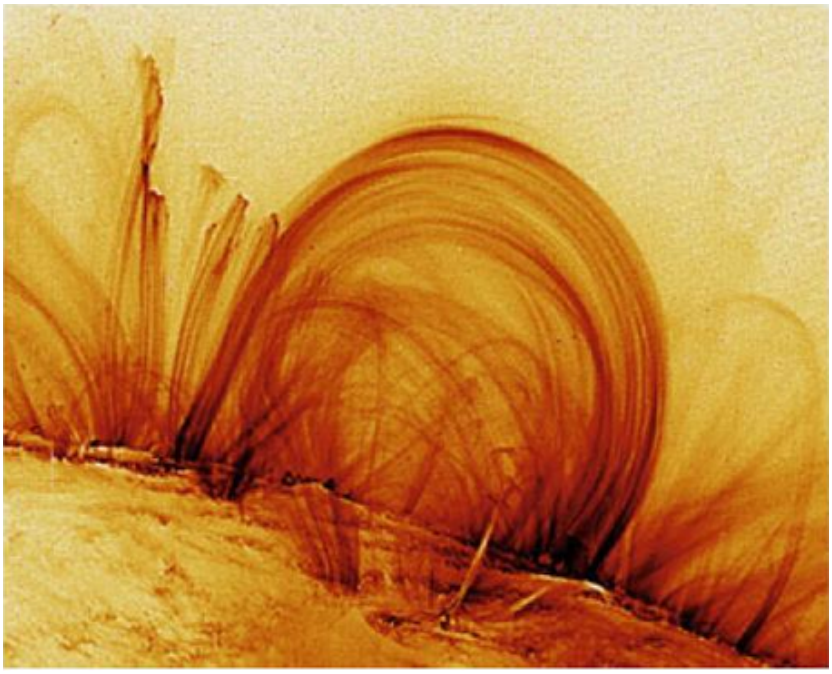

Figure 1.4: Image of the solar surface and coronal loops taken in extreme ultraviolet light by the TRACE satellite. Taken from [28].

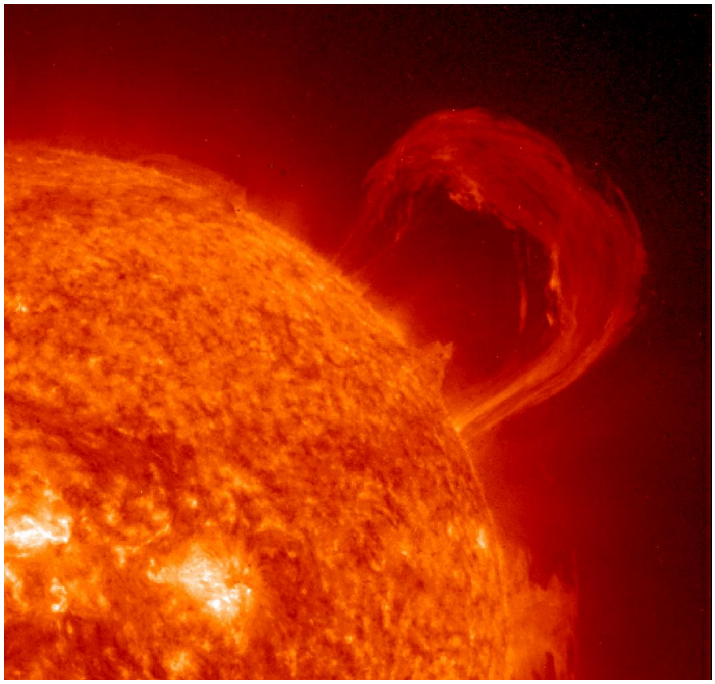

Figure 1.5: Image of an erupting prominence taken by SoHO spacecraft's Extreme Ultraviolet Imaging Telescope. Taken and edited from [33].

1.1.2 Explosive phenomena in the solar atmosphere

In the solar atmosphere, explosive phenomena, such as solar flares and coronal mass ejections, take place in a matter of seconds to hours [2]. These events occur due to the energy release by magnetic reconnection (the process when magnetic field lines in plasma break and realign) [34] and are particularly explosive when the Sun is at the maximum phase of the Solar activity cycle [2].

Solar flares are the most explosive form of solar activity. These are sudden releases of energy leading to the enhancement of electromagnetic radiation over a very wide spectrum and motion of mass, particles and waves. In a large flare, 10^{25} J of energy may be released. At ground-based observatories, flares are observed as sudden chromospheric brightening [2].

Coronal mass ejections (CMEs) – see Fig. 1.6 – are expulsions of large clusters of plasma from the corona, which then travel into interplanetary space [17]. They are associated with prominence eruptions and are often accompanied by large flares [41]. These discharges are a significant source of solar wind in the equatorial region. The ejected plasma clusters can have different dimensions and velocities. Some are in the form of loops or bubbles or have an

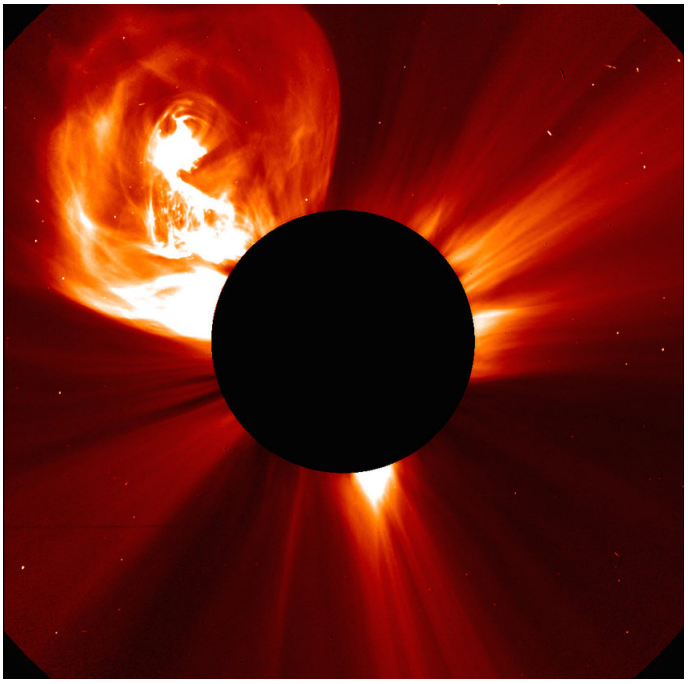

Figure 1.6: A CME (in the upper left) captured on 4th January 2002 by the SOHO/LASCO C2 coronograph. The view of the solar disk is blocked by an occulting disk with a radius of $1.7R_{\odot}$, where $R_{\odot}$ is the solar radius. Taken from [20].

irregular shape. Their mass ranges from 10^{12} to 10^{13} kg, the propagation speed usually reaches 200–500 $\mathrm{km} \cdot \mathrm{s}^{-1}$ [17].

1.1.3 Coronal waves

Plasma waves are ubiquitous in the cosmic plasma and are also observed in the solar plasma [43]. These include Alfvén waves, which cause transverse waves of the magnetic field, not causing density changes in the medium. Furthermore, magnetoacoustic waves can propagate in plasma. These, in turn, are conditioned by its compressibility [9] and can be considered as sound waves modified by the magnetic field of the environment [34].

Magnetoacoustic waves are divided into slow and fast magnetoacoustic waves according to the direction of their movement with respect to the magnetic field lines. The slow are very anisotropic and cannot move perpendicularly to the magnetic field lines, while the fast are almost isotropic, however, they move a little easier perpendicularly to the magnetic field lines [23].

The phase velocity distribution of the Alfvén and fast and slow magnetoacoustic waves can be plotted by a Friedrichs diagram [24] – see Fig. 1.7. These waves, also called magnetohydrodynamic (MHD) waves, have a spatial scale much larger than the ion gyroradii and a time scale much larger than the ion gyroperiods, and they are non-relativistic. Therefore, they can be described by the MHD approach, where the plasma is viewed as an electrically conductive fluid and the MHD equations describe its motion (see Sec. 2.3). MHD waves, as well as magnetic reconnection, are one of the general model classes of heating of the chromosphere and corona [34].

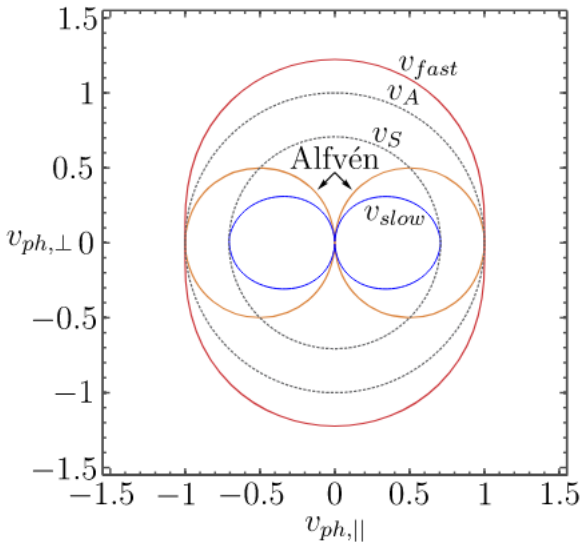

Figure 1.7: A Friedrichs diagram plotted for $v_s > v_A > v_f$, where v_s, v_A and v_f are the velocities of slow magnetoacoustic waves, Alfvén waves and fast magnetoacoustic waves, respectively, showing the distribution of their phase velocity components parallel and perpendicular to the equilibrium magnetic field. Taken from [24].

In the solar corona, magnetoacoustic waves can be observed in several modes. Structures of a cylinder-like form, and therefore also magnetic structures in the corona, are very good waveguides for acoustic or magnetoacoustic waves. Such structures are also quite commonly found in laboratory plasma and are called pinches [23].

The magnetoacoustic waves in the solar corona can be either standing or progressive. Standing waves can be observed in closed magnetic structures, while progressive waves can be observed in open or locally in closed structures (in parts of long coronal loops when the wave has not bounced from the loop footpoint) [23].

Coronal waves can also be either longitudinal or transverse. The simplest longitudinal waves are called sausage mode waves, these are symmetrical perturbations in magnetic structures which do not disturb the symmetry axis [23]. An intensively studied example of transverse coronal waves are kink mode waves [31]. Fig. 1.8 shows a transverse section of a loop in kink mode at two different phases. Fig. 1.9 shows a longitudinal section of a progressive and standing kink mode wave.

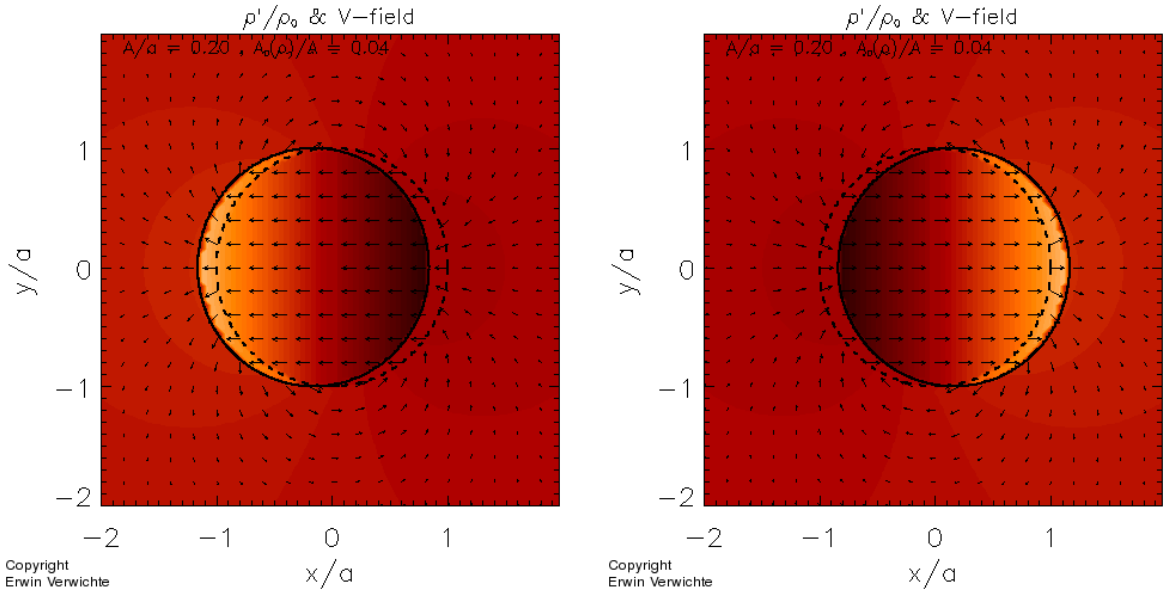

Figure 1.8: A transverse section of a coronal loop modelled as a straight cylinder in kink mode at two different phases, displaying the density perturbation and velocity field. The dashed circle shows the original profile of the loop. Taken from [40].

Kink mode waves were first observed by the TRACE satellite on 14th July 1998 as oscillating displacements of coronal loops shortly after a solar flare, and these oscillations were most likely generated by it [32]. Since then, kink mode waves in coronal loops have been observed many times in association with solar flares and CMEs, and more observational evidence of their role in the excitation of these waves has been obtained [25, 44]. Furthermore, in [31], the possible role of vortex shedding (see Sec. 1.2) in their excitation is discussed.

Prominences are also subject to oscillatory motions of various types that can be interpreted in terms of MHD waves. These oscillations have been classified according to different parameters, such as amplitude or period. The so-called large-amplitude oscillations (with velocity amplitudes given as $\geq 20\,\mathrm{km}\cdot\mathrm{s}^{-1}$) are often associated to an energic event that leads to os-

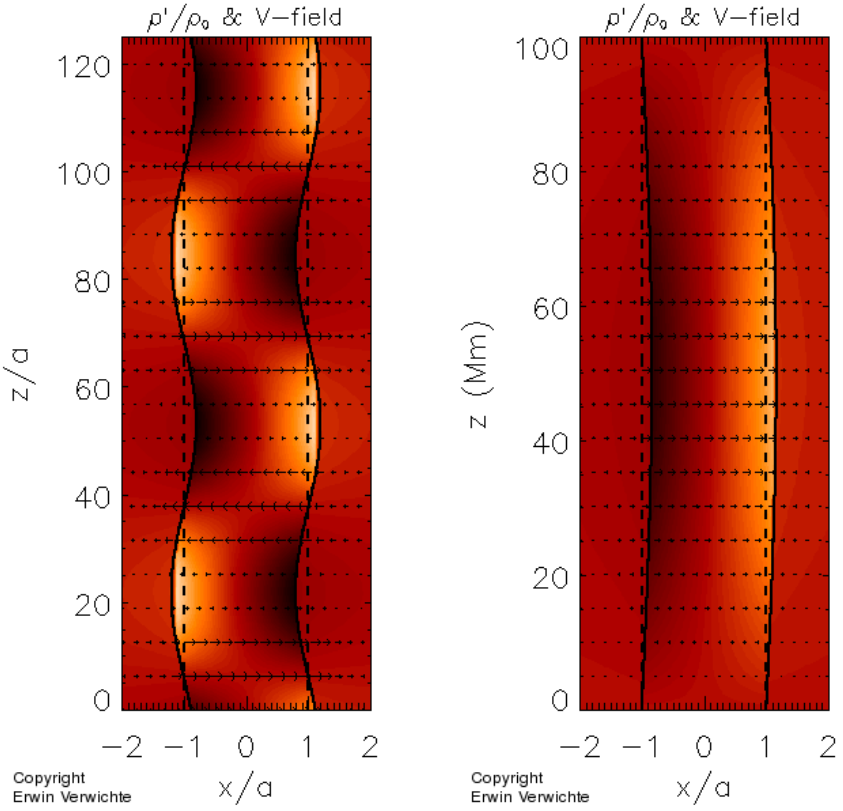

Figure 1.9: Longitudinal sections of a coronal loop modeled as a straight cylinder in kink mode, displaying the density perturbation and velocity field – a progressive wave (on the left) and a standing wave (on the right). The dashed lines show the original profile of the loop. Taken from [40].

cillation in the whole prominence or its large part. The so-called small-amplitude oscillations (with velocity amplitudes given as $\leq 3\,\mathrm{km}\cdot\mathrm{s}^{-1}$) generally affect only a small volume of the prominence [4] and are a much more common phenomenon [39]. The characteristic oscillation periods can be classified in these ranges: ≤ 1 min, $\leq$ 1–20 min, $\leq$ 20–40 min and $\leq$ 40–100 min, which are referred to as very short, short, intermediate and long [7].

1.2 Vortex shedding

Over a wide range of Reynolds number values, fluid flow around bluff bodies, such as a cylinder (with the longitudinal axis perpendicular to the flow direction), leads to the formation of a chain of vortices that form just behind the obstacle and disconnect from it alternately from each side. This periodic vortex formation is called vortex shedding. The regular chain created

as a result of this phenomenon – see Fig. 1.10 – is then called Kármán vortex street after the American scientist of Hungarian origin Theodor von Kármán (1881–1963) [42].

This phenomenon has been widely studied in hydrodynamic conditions in both science and mechanical engineering. It has also been studied by some numerical simulations in magnetic field environments, mainly in two spatial dimensions, see, for example, [12, 22, 36]. Observations suggest the possibility of its occurrence in the solar atmosphere [35]. For example, radial and azimuthal oscillations that may be related to self-oscillating processes such as vortex shedding have been observed in CMEs [29]. Furthermore, it is a possible mechanism for excitation of kink mode oscillations in coronal loops [31]. In magnetohydrodynamic conditions, however, it is less well understood [22] and its direct observational evidence is still missing [35].

The vortex shedding frequency f depends on the flow velocity v and the obstacle characteristic dimension (in this case, on the inner diameter of the loop d). These parameters are linked by the Strouhal number, named after the Czech experimental physicist Vincenc Strouhal (1850–1922) [22]:

$$St = \frac{fd}{v}. \tag{1.1}$$

During fluid flow around a cylindrical body in hydrodynamic conditions, St is around 0.2 for a wide range of Re values [42]. It has not been systematically and in detail examined in magnetic field environments [22], but has been observed in some numerical simulations, see for example [12, 22], where it was also close to the stated value.

Article [31] presents a model explaining the possibility of excitation of kink mode oscillations in coronal loops by the vortex shedding phenomenon. In this model, the bluff obstacle is presented by the upper, horizontal section of a cylindrical coronal loop surrounded by vertical flow originating from a CME. These conditions can cause vortex shedding, which periodically exerts a force on the loop, alternately from each side. If the magnetic field of the plasma flowing around the loop is parallel to its axis, this force is perpendicular to the loop axis and the flow direction, as indicated in Fig. 1.11. The loop is then periodically moved horizontally by this force and returned to the equilibrium position. If this force resonates with the natural frequency of the loop, kink mode oscillation is excited [31]. This mechanism was numerically studied in a 3D MHD model in [26].

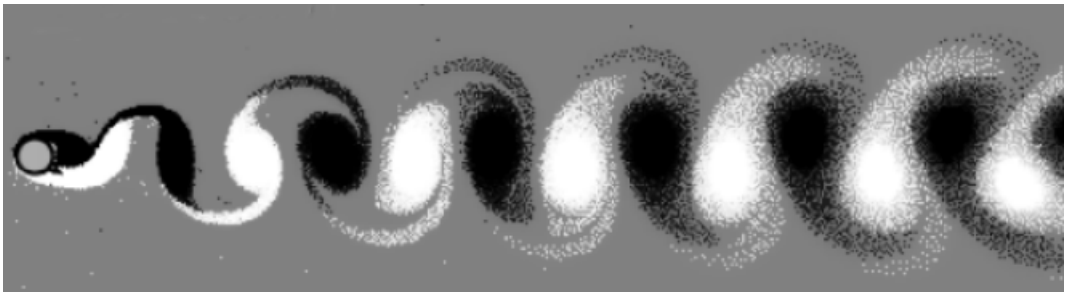

Figure 1.10: Simulation of the Kármán vortex street phenomenon behind a cylindrical body. Taken and edited from [14].

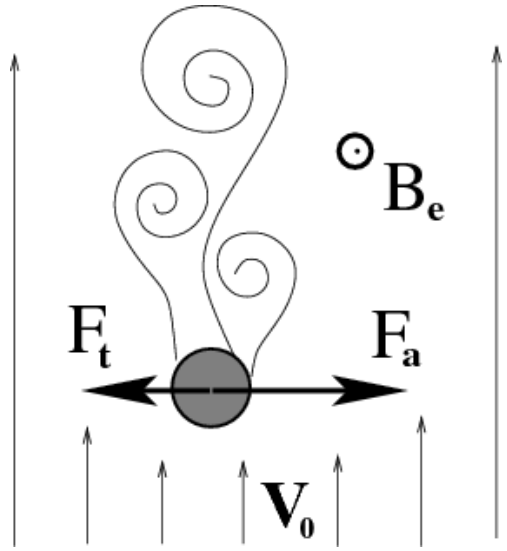

Figure 1.11: Excitation of transverse waves in coronal loops at vertical flow caused by CME and the subsequent vortex shedding. The grey circle represents the cross-section of the top of the loop. The vertical arrows indicate the flow direction at velocity v_0. The external magnetic field B_e is oriented parallel to the magnetic field of the loop section. Forces F_a, F_t periodically act on the loop in the horizontal direction. Taken from [31].

2 Numerical models

2.1 Numerical code Lare3d

The numerical simulations in this thesis were performed using the numerical code Lare3d[1] (Lagrangian remap 3D code). It is a freeware numerical code used to solve the MHD equations in three spatial dimensions. It was developed at the University of Warwick in the Fortran 90 programming language. The code also exists in the variant for 2D simulations under the name Lare2d. Both codes are collectively referred to as LareXd [3].

The code uses the Lagrangian-remap method (see schematic in Fig. 2.1), splitting each timestep into a Lagrangian step followed by a remap step [3], which does not involve adapting the grid resolution. When the medium is deformed, the grid evolves according to the fluid flow that caused this deformation. After that, the grid is remapped onto its original state, which (apart from the interpolation inaccuracies) does not affect the fluid variables and only transfers them to the cells of the remapped grid [21].

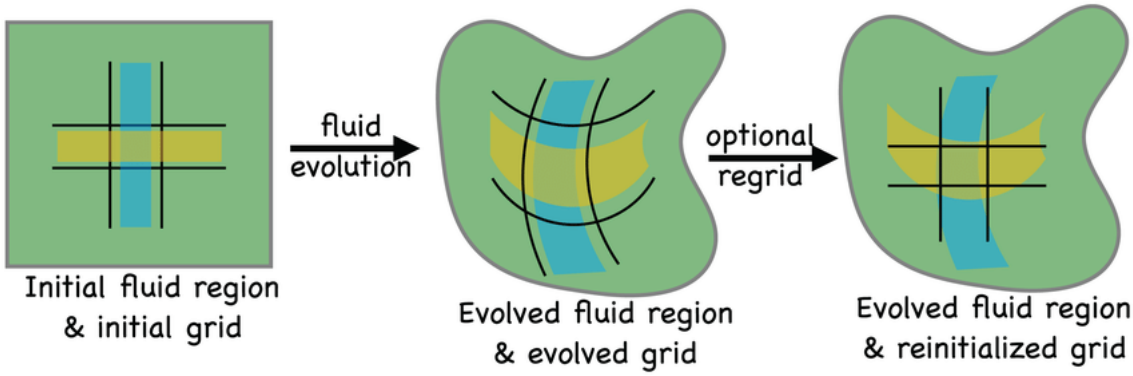

Figure 2.1: A schematic of the Lagrangian-remap method. Taken from [21].

[1] https://warwick.ac.uk/fac/sci/physics/research/cfsa/people/tda/larexd/

The grid and structure of numerical code Lare2d are already described in bachelor thesis [8]. Hence only the difference between the grid of the Lare3d code and its two-dimensional variant is explained below.

The grid consists of $nx \times ny \times nz$ cells, denoted by coordinates ix, iy and iz. As in the numerical code Lare2d, a staggered grid is used here, which means different positions at the cell are used to define different types of variables. This grid in three dimensions is illustrated in Fig. 2.2.

The coordinates of the cell vertices are variables xb_i, yb_i and zb_i (boundary), while the cell centre coordinates are variables xc_i, yc_i and zc_i (centre). Therefore, for example, the B_y magnetic field component is defined at (xc_i, yb_i, zc_i). The gravitational acceleration is set in the z-axis direction and at the same position at the cell as the v_z velocity component [3].

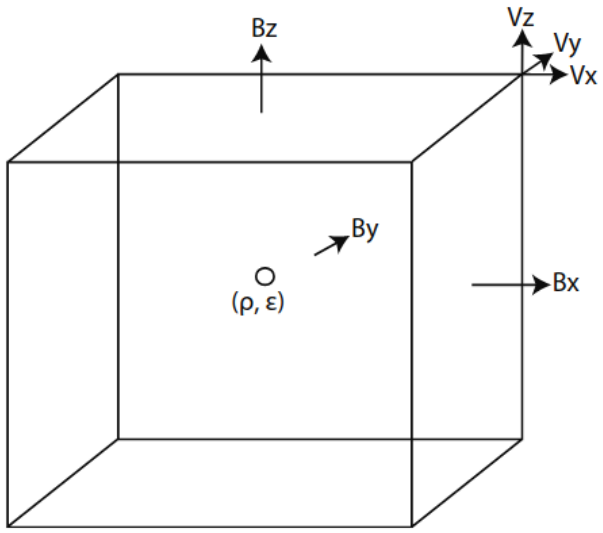

Figure 2.2: A cell of a 3D staggered grid. Scalars are defined at the centre, velocity components and gravitational acceleration are defined at the vertices, and magnetic field components are defined in the middle of the faces. Taken from [3].

2.2 Normalization

The normalizing constants used for magnetic field, density and length in the numerical simulations, which correspond to typical values in the solar corona, are defined as follows:

- $B = B_0\hat{B}$, $B_0 = 10\,\mathrm{G}$

- $\rho = \rho_0 \hat{\rho}$, $\rho_0 = 10^{-12}\,\mathrm{kg \cdot m^{-3}}$
- $x = L_0 \hat{x}$, $L_0 = 10^6\,\mathrm{m}$

The diacritical mark ˆ is used to distinguish quantities expressed in dimensionless form. The normalizing constants of other quantities are derived from these constants, as explained in the LareXd manual [3]. Below are the normalizing constants of velocity, time and temperature, including their derivation.

- $v_0 = \frac{B_0}{\sqrt{\mu_0 \rho_0}} = 8.92 \cdot 10^5\,\mathrm{m \cdot s^{-1}}$
- $t_0 = \frac{L_0}{v_0} = 1.12\,\mathrm{s}$
- $T_0 = \frac{\varepsilon_0 \bar{m}}{k_\mathrm{B}} = 1.16 \cdot 10^8\,\mathrm{K}$, where $\varepsilon_0 = {v_0}^2$ is the specific internal energy density normalizing constant and $\bar{m}$ is the average mass of ions in the plasma

2.3 Governing equations

The resistivity is not considered in our numerical simulations, so the fluid description was performed using the ideal MHD equations. They can be written in the following form:

$$\frac{\partial \rho}{\partial t} + \boldsymbol{\nabla} \cdot \rho \mathbf{v} = 0, \tag{2.1}$$

$$\rho \frac{\partial \mathbf{v}}{\partial t} + \rho (\mathbf{v} \cdot \boldsymbol{\nabla}) \mathbf{v} + \boldsymbol{\nabla} p - \frac{1}{\mu_0} (\boldsymbol{\nabla} \times \mathbf{B}) \times \mathbf{B} = 0, \tag{2.2}$$

$$\frac{\partial p}{\partial t} + \mathbf{v} \cdot \boldsymbol{\nabla} p + \gamma p \boldsymbol{\nabla} \cdot \mathbf{v} = 0, \tag{2.3}$$

$$\frac{\partial \mathbf{B}}{\partial t} - \boldsymbol{\nabla} \times (\mathbf{v} \times \mathbf{B}) = 0, \tag{2.4}$$

$$\boldsymbol{\nabla} \cdot \mathbf{B} = 0, \tag{2.5}$$

where all the terms have their usual meaning or are also included in the List of symbols. Equation (2.5), one of the Maxwell's equations, expresses the absence of magnetic monopoles.

In the case of considering the solar gravitational field, Euler's equation of motion (2.2), in addition to the Lorentz force, expressed by the term $\frac{1}{\mu_0} (\boldsymbol{\nabla} \times \mathbf{B}) \times \mathbf{B}$, also includes the gravitational

force [18, 23] with $g_\odot = 274\,\mathrm{m}\cdot\mathrm{s}^{-2}$. This equation can then be written as follows:

$$\rho\frac{\partial \mathbf{v}}{\partial t} + \rho(\mathbf{v}\cdot\boldsymbol{\nabla})\mathbf{v} + \boldsymbol{\nabla}p - \frac{1}{\mu_0}(\boldsymbol{\nabla}\times\mathbf{B})\times\mathbf{B} - \rho\mathbf{g}_\odot = 0. \tag{2.6}$$

When the magnetic field is not considered, on the contrary, the Lorentz force is not calculated in the equation, and the induction equation (2.4) is not solved. Therefore, the equations change to the HD form.

In the simulations, fully ionized plasma was considered (and therefore $\gamma = \frac{5}{3}$) with an average mass of ions $\bar{m} = 1.2m_\mathrm{p}$ (and therefore an average particle mass of $0.6m_\mathrm{p}$), typical for solar corona [3].

2.4 Simulation box

Figure 2.3 illustrates the simulation box used and some settings common to all simulations. The simulation box has a size of $x \times y \times z$, where $x = 5\,\mathrm{Mm}$, $y = 5\,\mathrm{Mm}$, $z = 20\,\mathrm{Mm}$. It is composed of $100 \times 100 \times 400$ cells, so the space step length is $\Delta x = 0.05\,\mathrm{Mm}$, and the time step length Δt was computed throughout the simulations according to the Courant–Friedrichs–Lewy (CFL) condition [10]. There is a rigid stationary cylindrical obstacle with a centre at $\hat{x} = 0$, $\hat{y} = 0$, $\hat{z} = 5$, which was positioned so that its longitudinal axis was perpendicular to the flow plane. This obstacle represents the upper section of a magnetic structure, such as a prominence thread, which can be considered approximately a cylinder.

2.5 Boundary conditions

Because the simulation box represents a domain of a larger system, open boundaries were set on the x and z axes so that the fluid could move freely beyond them. Since the B_y magnetic field component was applied in each MHD simulation, as shown in Fig. 2.3, and open boundaries implemented in LareXd are only accurate if the magnetic field does not significantly change from the initial magnetic field [3], periodic boundary conditions had to be set on the y-axis.

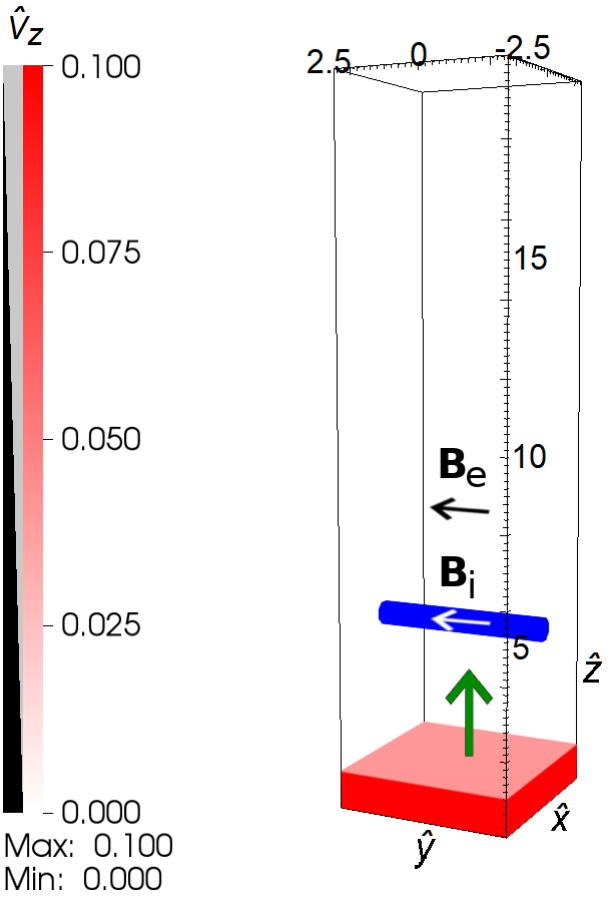

Figure 2.3: Initial velocity distribution and the magnetic field orientation inside and out of the cylindrical obstacle ($\mathbf{B}_i$, $\mathbf{B}_e$) in the initial state. The cylindrical obstacle is marked in blue. The green arrow indicates the initial flow direction.

3 Numerical simulations and results

The parametric study in this thesis includes one numerical simulation of flow past a cylindrical body under hydrodynamic (HD) conditions and five in a magnetic field environment, each with a different initial value of magnetic field constant throughout the simulation box, including the obstacle. It allowed us to evaluate the effect of the magnetic field on the frequency of the vortex shedding process. Another simulation was performed with the addition of a gravitational field and a stronger magnetic field inside the cylindrical body, which was supposed to make the model more consistent with the real coronal environment and magnetic structures. Each simulation lasted at least 1000 t_0 time units, the interval between the output snapshots is 5 t_0 time units.

3.1 Initial conditions

The parameters set in the initial conditions of each simulation, expressed in SI units, are summarized in Tab. 3.1 and will be explained in the following sections. The parameters of the cylindrical body roughly correspond to typical parameters of prominences inferred from SoHO measurements and other sources [5].

3.1.1 Flow speed

A cylindrical area with constant zero velocity was defined in the simulation box to introduce a rigid stationary cylindrical obstacle. Furthermore, a boundary condition was determined for the v_z velocity component of the fluid flowing from the bottom wall of the box in the z-axis direction. These speed conditions were set in the file `initial_conditions.f90` and also in

Table 3.1: Parameters set in the initial conditions of each simulation, expressed in SI units.

	HD	MHD	MHD with gravity
$\rho_e\ [\mathrm{kg \cdot m^{-3}}]$	10^{-12}	10^{-12}	10^{-12} (at $z = 5\,\mathrm{Mm}$)
$\rho_i\ [\mathrm{kg \cdot m^{-3}}]$	10^{-11}	10^{-11}	10^{-11}
$T_e\ [\mathrm{K}]$	$2 \cdot 10^6$	$2 \cdot 10^6$	$2 \cdot 10^6$
$T_i\ [\mathrm{K}]$	$2 \cdot 10^5$	$2 \cdot 10^5$	$2 \cdot 10^4$
$B_{y_e}\ [\mathrm{T}]$	0	10^{-4} $2 \cdot 10^{-4}$ $3 \cdot 10^{-4}$ $4 \cdot 10^{-4}$ $5 \cdot 10^{-4}$	10^{-4}
$B_{y_i}\ [\mathrm{T}]$	0	10^{-4} $2 \cdot 10^{-4}$ $3 \cdot 10^{-4}$ $4 \cdot 10^{-4}$ $5 \cdot 10^{-4}$	$2.268 \cdot 10^{-4}$
$r^2\ [\mathrm{m^2}]$	10^{11}	10^{11}	10^{11}
$v_{z_{\mathrm{init}}}\ [\mathrm{m \cdot s^{-1}}]$	$8.921 \cdot 10^4$	$8.921 \cdot 10^4$	$8.921 \cdot 10^4$
$g_\odot\ [\mathrm{m \cdot s^{-2}}]$	0	0	274

`lagran.F90` to apply at each time step. The following command was inserted in the appropriate blocks:

```
DO iz = -2,nz+2
 DO iy = -2,ny+2
  DO ix = -2,nx+2
   IF ((xb(ix)**2.0_num + (zb(iz)-z_pos)**2.0_num).le.(r_2)) THEN
    vx(ix, iy, iz) = 0.0_num
    vy(ix, iy, iz) = 0.0_num
    vz(ix, iy, iz) = 0.0_num
   END IF
```

```
    IF (zb(iz).le.v_pos) THEN
     vz(ix,iy,iz) = v_init
    END IF
   END DO
  END DO
END DO
```

Variables `z_pos`, `r_2` ($\hat{r}^2$), `v_init` ($\hat{v}_{z_{\text{init}}}$) and `v_pos` represent the position of the cylinder centre on the z-axis, the square of the cylinder radius, the velocity of the fluid advancing from the bottom wall of the box in the z-axis direction and the farthest position on the z-axis for which this velocity applies, respectively. The initial velocity in the rest of the box was left at zero.

As shown in Fig. 2.3, variable `v_pos` was set to 1. Because near the position corresponding to value `v_pos` there is a sharp increase in velocity at the beginning of the simulation, causing significant numerical errors, it was necessary to choose a high enough value for `z_pos` to prevent these errors from occurring near the cylindrical obstacle. Therefore, a value of 5 was chosen.

This flow mimics a CME. Although its speed can take on a wide range of values, variable $v_{z_{\text{init}}}$ was set so that it did not exceed the characteristic velocity in the given environment, which is the speed of sound for HD conditions and the Alfvén speed for MHD conditions. Therefore, no shock waves were generated, which could lead to significant numerical errors due to the resolution used.

3.1.2 Mass density

Variable ρ_{e} in Tab. 3.1 expresses the initial mass density in the entire volume of the box outside the cylindrical obstacle, except in the case of the gravitational field.

In the simulation with a gravitational field, mass density stratification of the solar atmosphere with the initial state according to the following relation was considered:

$$\rho(h) = \rho(0) \cdot \exp\left(-\frac{h}{\lambda}\right), \tag{3.1}$$

where $\lambda = \frac{k_B T}{\mu m_p g_\odot}$ is the pressure scale height [5] and h is the considered height. For application to the numerical simulations, this relation was converted to a dimensionless form, expressed as follows:

$$\hat{\rho}(\hat{h}) = \hat{\rho}(0) \cdot \exp\left(\frac{-\mu \hat{g}_\odot \hat{h}}{\hat{T}}\right), \tag{3.2}$$

where $\mu = 0.6$, $\hat{\rho}(0) = \hat{\rho}_e$ and the height $\hat{h}$ expresses the position on axis z subtracted by the value `z_pos`. Therefore, in the simulation with a gravitational field, $\hat{\rho}_e$ is the initial density at height `z_pos`.

Next, it was necessary to set the mass density inside the cylindrical obstacle ($\hat{\rho}_i$) for which variable `rho_in` was introduced. These initial conditions were introduced into the file `initial_conditions.f90` using the following cycle:

```
DO ix = -1, nx+2,
 DO iy = -1, ny+2
  DO iz = -1, nz+2
   rho(ix,iy,iz) = rho_0 * exp(-0.6_num * grav(iz) * (zc(iz) - z_pos) /
    ↪  temperature(ix,iy,iz))
   IF ((xc(ix)**2.0_num + (zc(iz)-z_pos)**2.0_num).le.(r_2)) THEN
    rho(ix,iy,iz) = rho_in
   END IF
  END DO
 END DO
END DO
```

A corresponding command was also included in the `lagran.F90` file to keep the density inside the obstacle constant throughout the simulation.

3.1.3 Magnetic field

In the case of considering a magnetic field, only its y component, perpendicular to the flow plane, was introduced (see Fig. 2.3).

As shown in Tab. 3.1, the magnetic fields inside and outside the cylinder (B_{y_i} and B_{y_e}, respectively) in the MHD simulations in a gravity-free medium are always equal. In this case, the constant initial magnetic field will be referred to as B_y.

3.1.4 Equilibrium condition

The equilibrium equation for media with the presence of magnetic forces reads [9]:

$$\nabla\left(p+\frac{B^2}{2\mu_0}\right)=\frac{1}{\mu_0}(\mathbf{B}\cdot\nabla)\cdot\mathbf{B}. \tag{3.3}$$

For the initial state of the simulations, when the right side of Eq. (3.3) is zero, the equilibrium equation is expressed as:

$$p+\frac{B^2}{2\mu_0}=\text{const.}, \tag{3.4}$$

which means the sum of the gas and magnetic pressures:

$$p=\frac{\rho k_\mathrm{B} T}{\mu m_\mathrm{p}},\ p_\mathrm{mag}=\frac{B^2}{2\mu_0},$$

respectively, is constant. Hence, it was necessary to set the initial sum of gas and magnetic pressure outside the cylinder to the same value as inside the cylinder. For that, the temperature inside the cylinder T_i had to be adjusted according to the initial ambient temperature T_e and other setpoints appearing in the latter relations. It was also introduced into the `lagran.F90` file to keep constant throughout the simulation.

3.2 Numerical data processing

LareXd numerical code includes packages that allow access to simulation outputs in VisIt[1] and IDL programming language[2] [3], which were used in this thesis.

3.2.1 Vorticity

The numerical simulations were graphically represented in the VisIt software. To visualize the evolution of the flow, including the formation of vortices, a colormap of the y component of

[1] `https://wci.llnl.gov/simulation/computer-codes/visit/`

[2] `https://www.l3harrisgeospatial.com/Software-Technology/IDL`

vorticity $\boldsymbol{\omega}$, which characterizes the vortex structure of the drag at each point of the continuum, given by the relation:

$$\boldsymbol{\omega} = \boldsymbol{\nabla} \times \mathbf{v}, \tag{3.5}$$

in the plane $y = 0$ was created for each recorded time step. In the following chapters, selected cross-sections are presented for each simulation. The vorticity evolution recorded from each simulation can be viewed online on the movies accessible from the attached QR codes. The value of $\hat{\omega}_y$ is always expressed in units of $\hat{v}_{z_0}/\hat{d}$, so it is the same as after conversion to basic SI units and can also be referred to as ω_y in units of v_{z_0}/d.

3.2.2 Relative density change

The density evolution was processed to analyze the vortex shedding period in IDL. From each simulation, the evolution of the relative density change ($\Delta\rho/\rho_0$) along axis x at $y = 0$ and a selected position on axis z through which each vortex passed was recorded.

After the graphical display of the $\Delta\rho/\rho_0$ time course by a colourmap, a suitable position on axis x was chosen and data were extracted from it (i.e. the $\Delta\rho/\rho_0$ time course in a single point was obtained). The vortex shedding period was determined from them using a software[3] for wavelet analysis [16, 38] in the MATLAB programming environment. It was necessary to choose a suitable position for determining the period of vortex pair formation, where the density changes caused by the formation of vortices did not interfere too much with minor density changes.

The values obtained were verified by testing the calculation on different positions. Selected graphs are presented in the following chapters for each simulation.

3.2.3 Strouhal number calculation

The Strouhal number at each simulation was calculated according to Eq. (1.1). Since the flow velocity decreases with the height, in this equation, v was taken as the average speed at $\hat{x} = -\hat{r}$, $\hat{y} = 0$, $\hat{z} = 4.65$ and $\hat{x} = \hat{r}$, $\hat{y} = 0$, $\hat{z} = 4.65$, i.e. close under the obstacle, but far enough from

[3] `http://atoc.colorado.edu/research/wavelets/`

its edge so it does not to approximate to zero. The velocity values were extracted using IDL as well.

3.3 Simulation in HD conditions

Figure 3.1 shows the distribution of ω_y at four time steps in the simulation with a zero magnetic field. The first graph shows the beginning of the vortex shedding process when the first

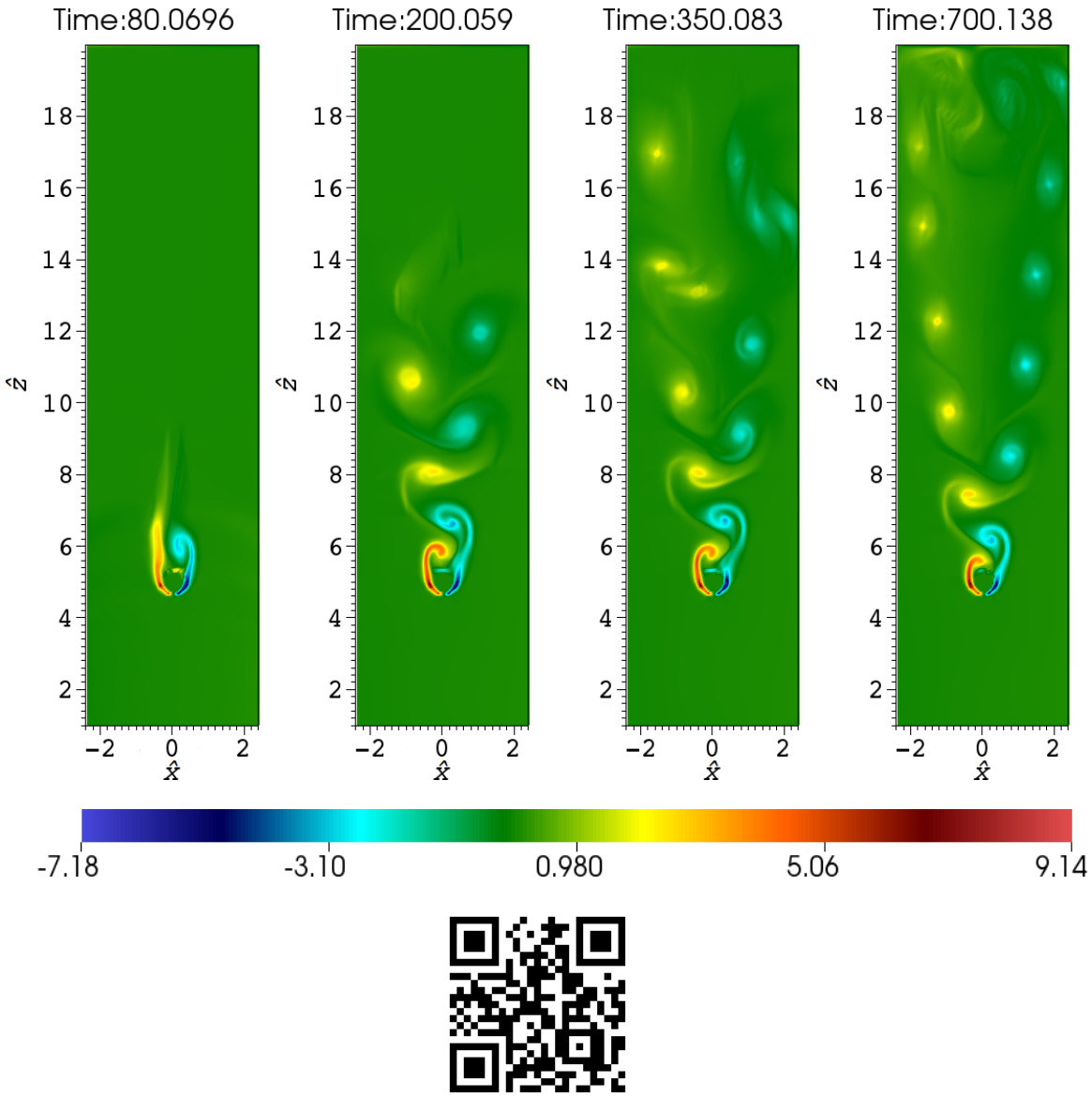

Figure 3.1: Evolution of the ω_y distribution in the units of v_{z_0}/d in the simulation in HD conditions. The whole process can be viewed online in the movie linked to the attached QR code.

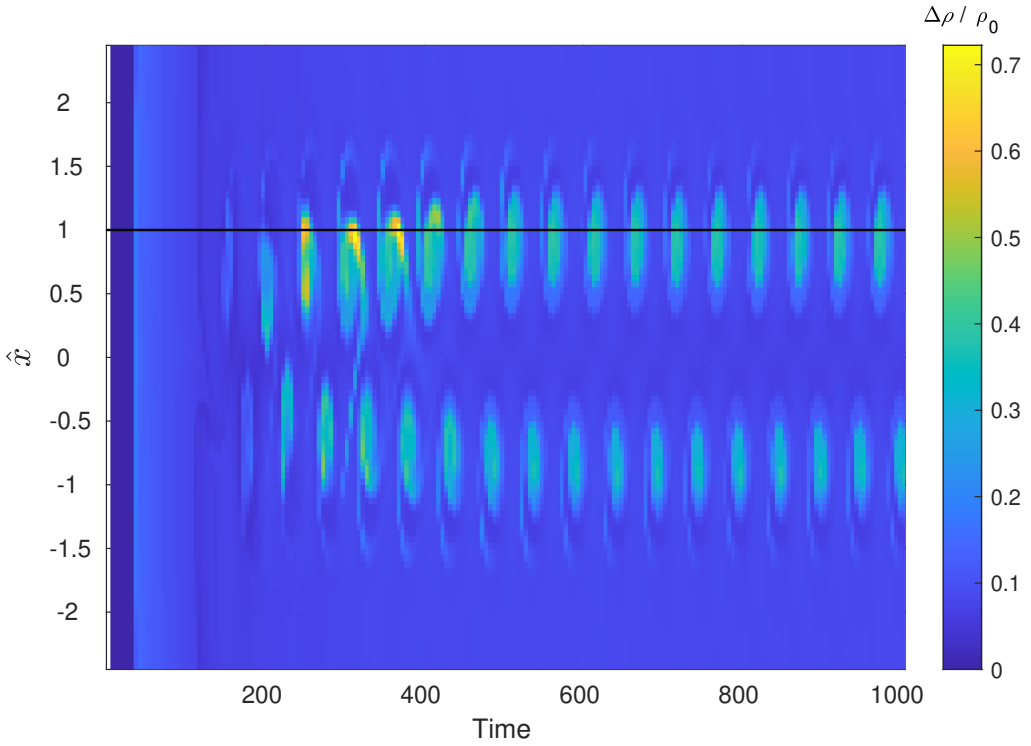

Figure 3.2: Evolution of $\Delta\rho/\rho_0$ along axis x at $\hat{y} = 0$, $\hat{z} = 9$ in the simulation in HD conditions. The black line indicates the x position to which Fig. 3.3 refers.

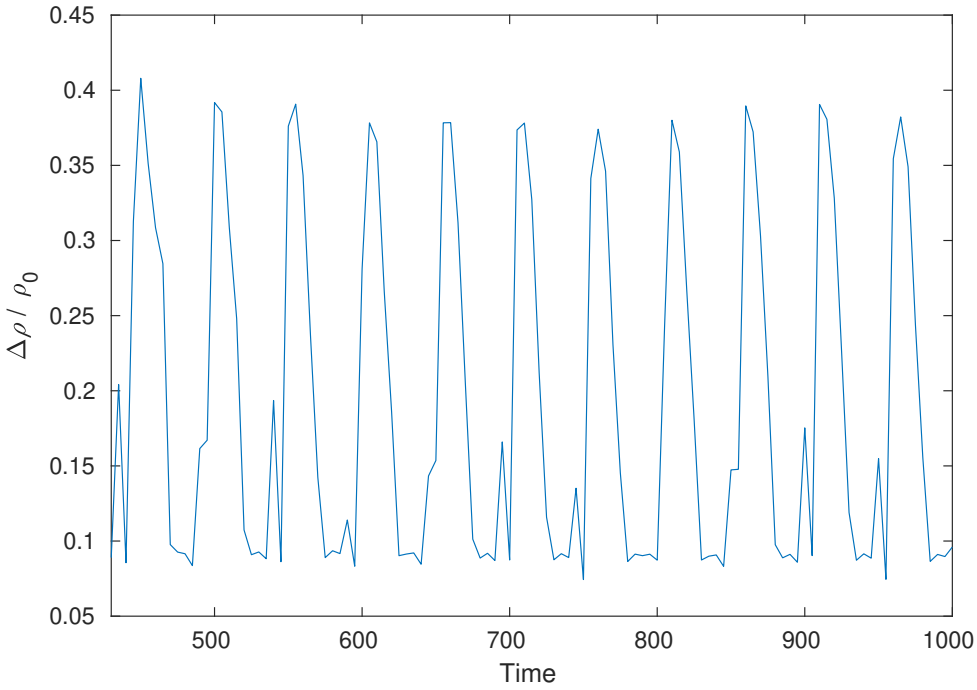

Figure 3.3: Evolution of $\Delta\rho/\rho_0$ at $\hat{x} = 1$, $\hat{y} = 0$, $\hat{z} = 9$ in the simulation in HD conditions. The range that was used to calculate St is displayed.

vortex is about to detach. A structured chain of vortices, i.e. Kármán vortex street, can be seen already in the second graph. The last graph shows the drag in its developed state. The attached movie shows that the vortex shedding process begins almost immediately after the flow reaches the cylindrical obstacle, without the creation of a symmetrical pair of vortices. The whole simulation lasts until $\hat{t} = 1000$.

Figure 3.2 shows the evolution of the relative density change $\Delta\rho/\rho_0$ along axis x at $\hat{y} = 0$, $\hat{z} = 9$ in this simulation. In Fig. 3.3 are plotted the data for $\hat{x} = 1$ in the range that was used to calculate St. The period value obtained from the evolution of $\Delta\rho/\rho_0$ is $\hat{P} = 51.23$. The average flow velocity value obtained as described in Sec. 3.2.3 is $\hat{v} = 0.0635$. The Strouhal number value $St = 0.1945$ was calculated.

3.4 Simulations with a constant initial magnetic field

Figures 3.4 to 3.8 show the distribution of ω_y at four time steps, the same as in Fig. 3.1, for each of the simulations.

Unlike in the case with a zero magnetic field (Fig. 3.1), two symmetrical vortices are visible in the first graphs in Figs. 3.4 to 3.8. As the value of B_y increases, their distance from the obstacle is greater. A structured chain of vortices, i.e. Kármán vortex street, can be seen only in the last graphs, which indicates that applying the magnetic field led to a delay in vortex shedding. Also, a change in the structure of the vortices can be seen in these graphs – they are larger and have lower vorticity values.

The delay in vortex shedding and the acquisition of lower ω_y values depending on the B_y value is better seen in the attached movies, where the minimum and maximum values of ω_y are documented for each output snapshot. Furthermore, unlike in the case of a zero magnetic field, where the vortex shedding process begins almost immediately after the flow reaches the obstacle, a chaotic turbulent flow takes place for some time, which can also be seen in the figures. By comparing the movies, it can also be seen that increasing the value of B_y reduces the vortex shedding frequency.

Since increasing the value of B_y led to a delay in vortex shedding, the simulations had to be prolonged depending on B_y to provide enough data capturing this process. This was primarily

important for analyzing its frequency as described in Sec. 3.2.2. Therefore, the simulation with $\hat{B}_y = 0.1$ lasted until $\hat{t} = 1500$, the simulations with $\hat{B}_y = 0.2$ and $\hat{B}_y = 0.3$ lasted until $\hat{t} = 1600$ and the simulations with $\hat{B}_y = 0.4$ and $\hat{B}_y = 0.5$ lasted until $\hat{t} = 1700$.

Figures 3.9, 3.11, 3.13, 3.15 and 3.17 show the evolution of the relative density change $\Delta\rho/\rho_0$ along axis x at $\hat{y} = 0$, $\hat{z} = 9$ in each of these simulations. In Figs. 3.10, 3.12, 3.14, 3.16 and 3.18 are plotted the data for a chosen x position in the range that was used to calculate St.

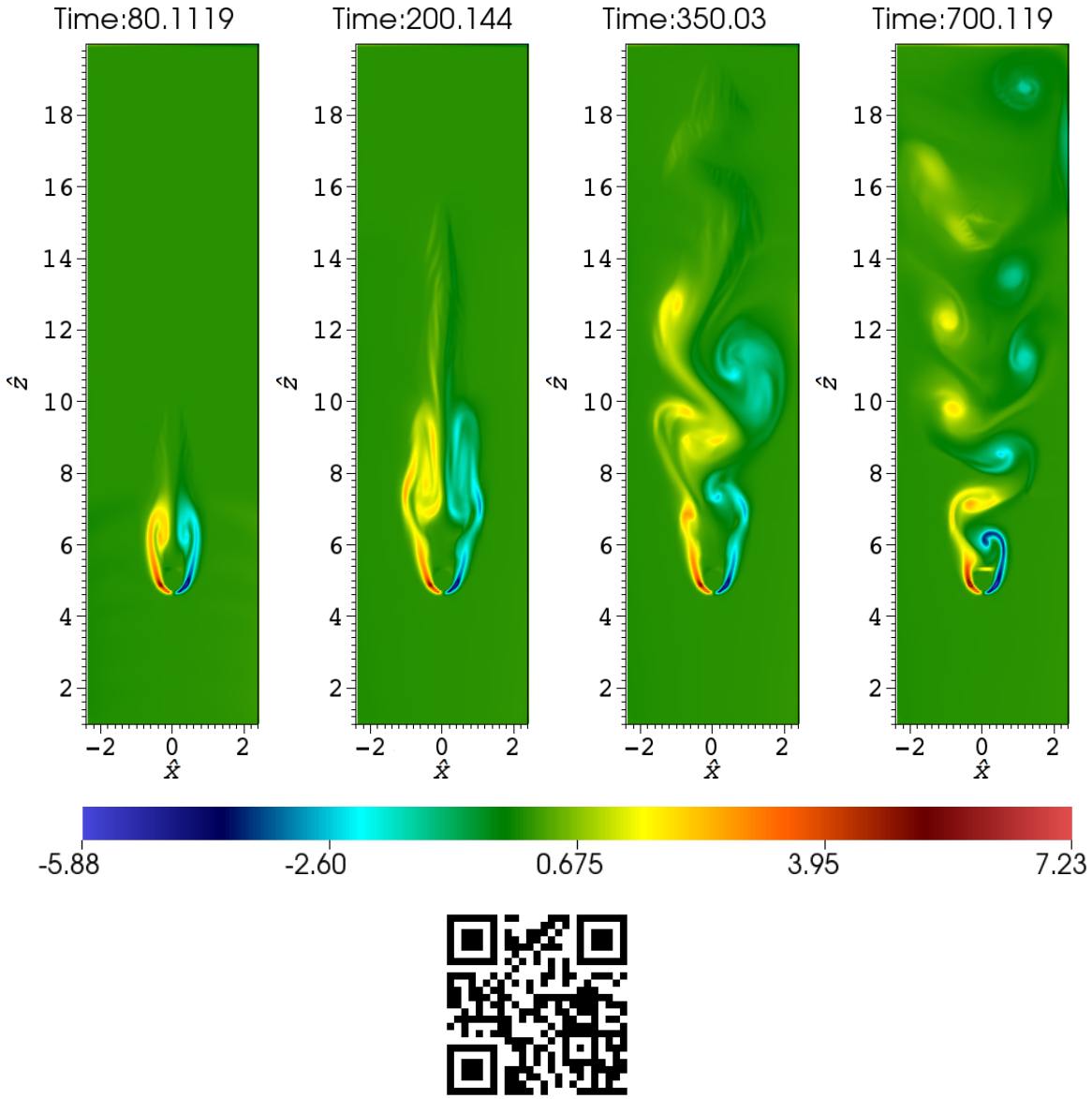

Figure 3.4: Evolution of the ω_y distribution in the units of v_{z_0}/d in the simulation with $\hat{B}_y = 0.1$. The whole process can be viewed online in the movie linked to the attached QR code.

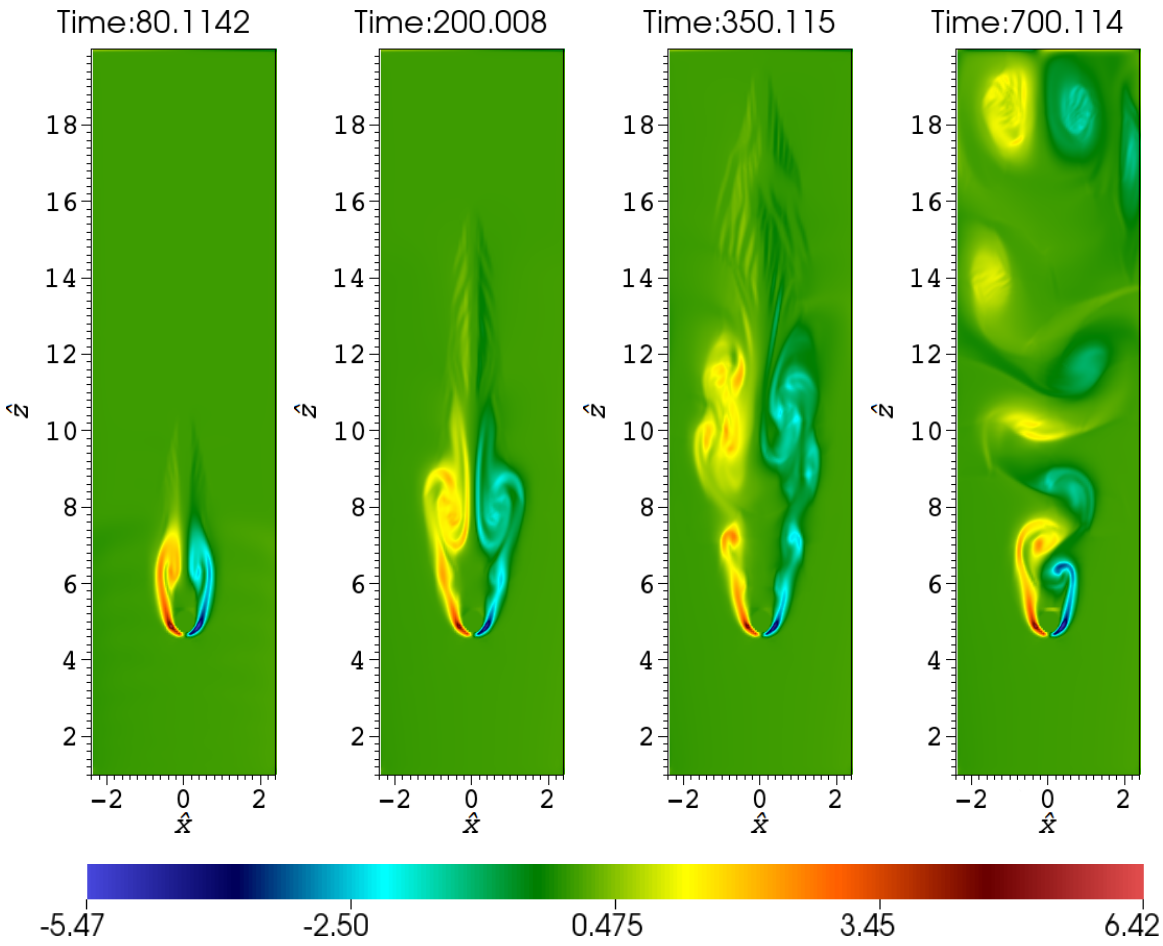

Figure 3.5: Evolution of the ω_y distribution in the units of v_{z_0}/d in the simulation with $\hat{B}_y = 0.2$. The whole process can be viewed online in the movie linked to the attached QR code.

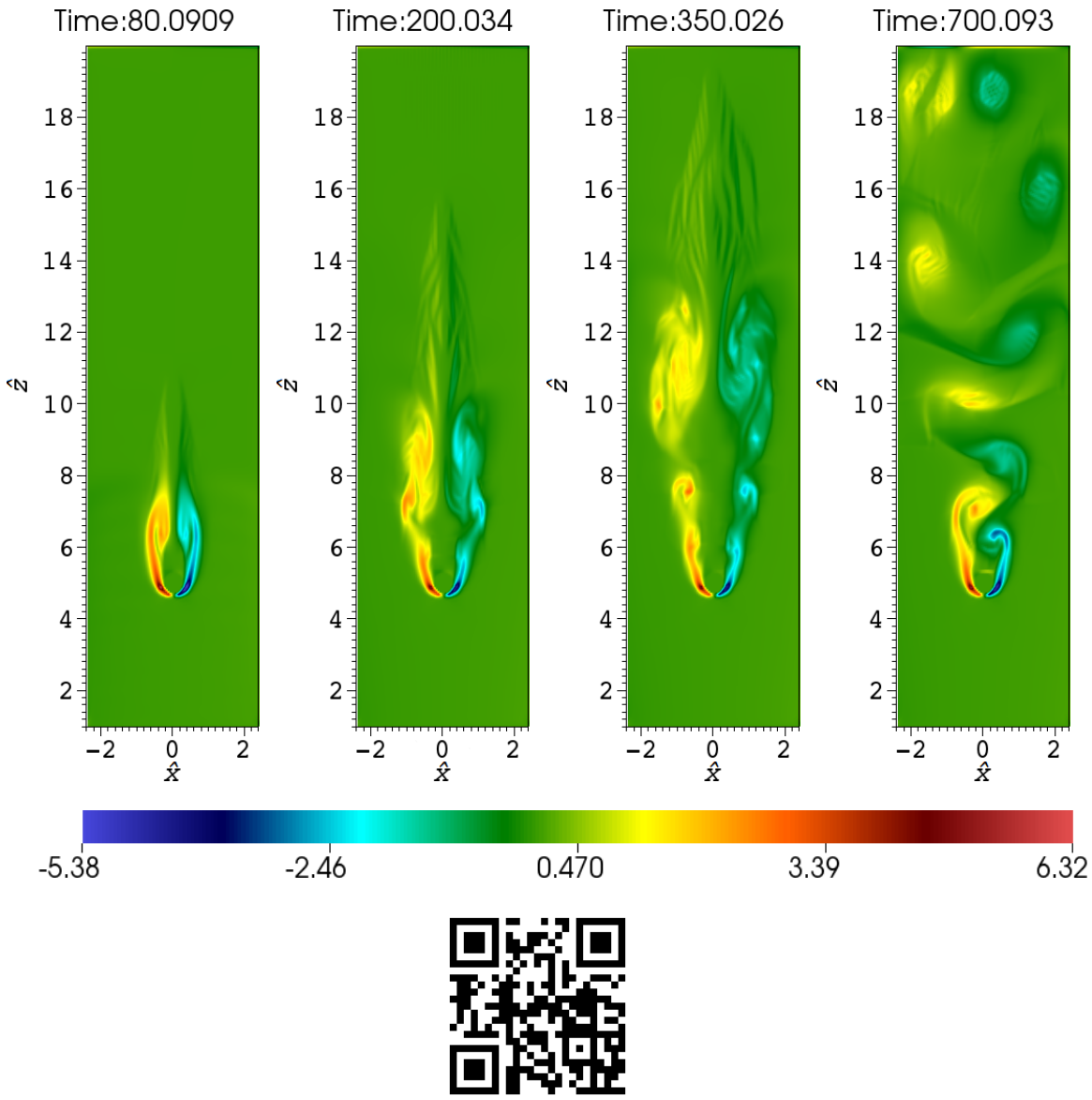

Figure 3.6: Evolution of the ω_y distribution in the units of v_{z_0}/d in the simulation with $\hat{B}_y = 0.3$. The whole process can be viewed online in the movie linked to the attached QR code.

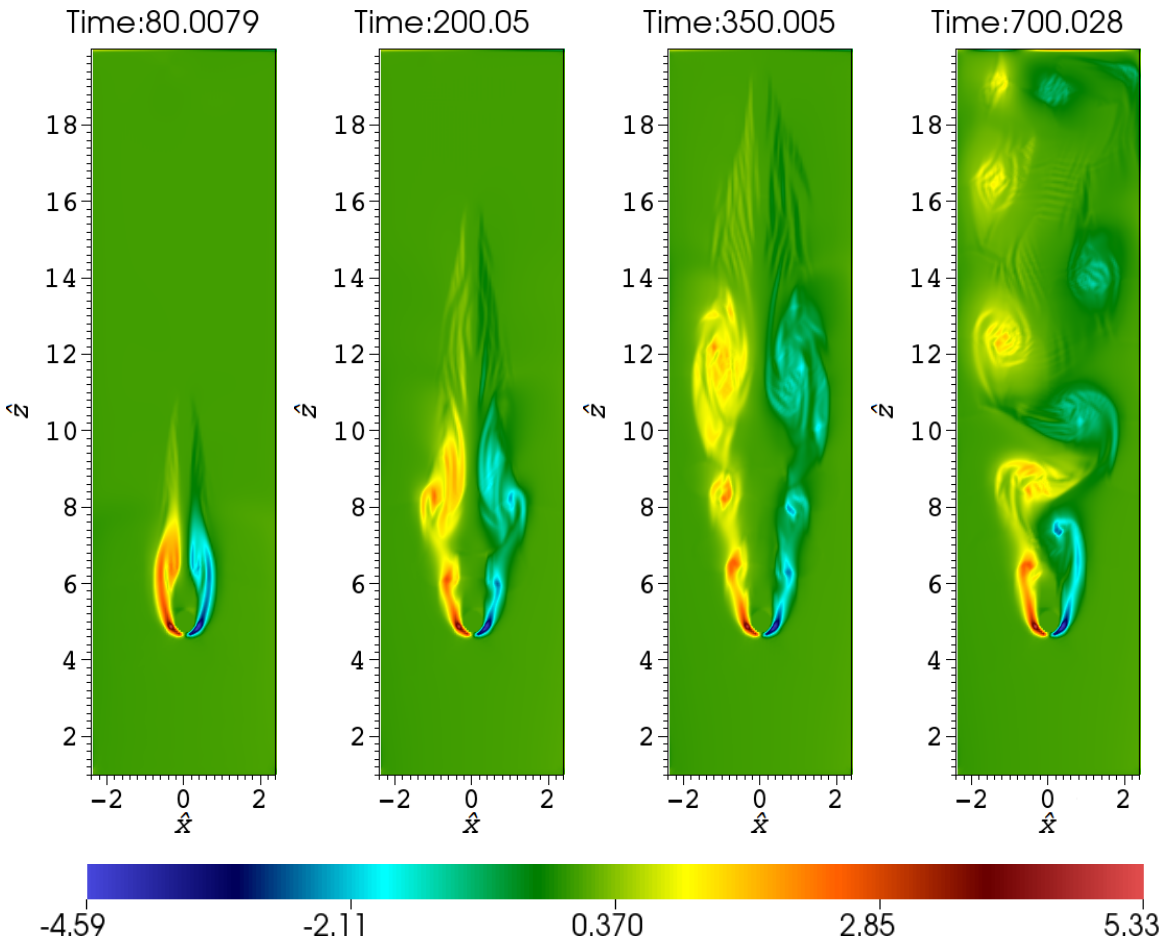

Figure 3.7: Evolution of the ω_y distribution in the units of v_{z_0}/d in the simulation with $\hat{B}_y = 0.4$. The whole process can be viewed online in the movie linked to the attached QR code.

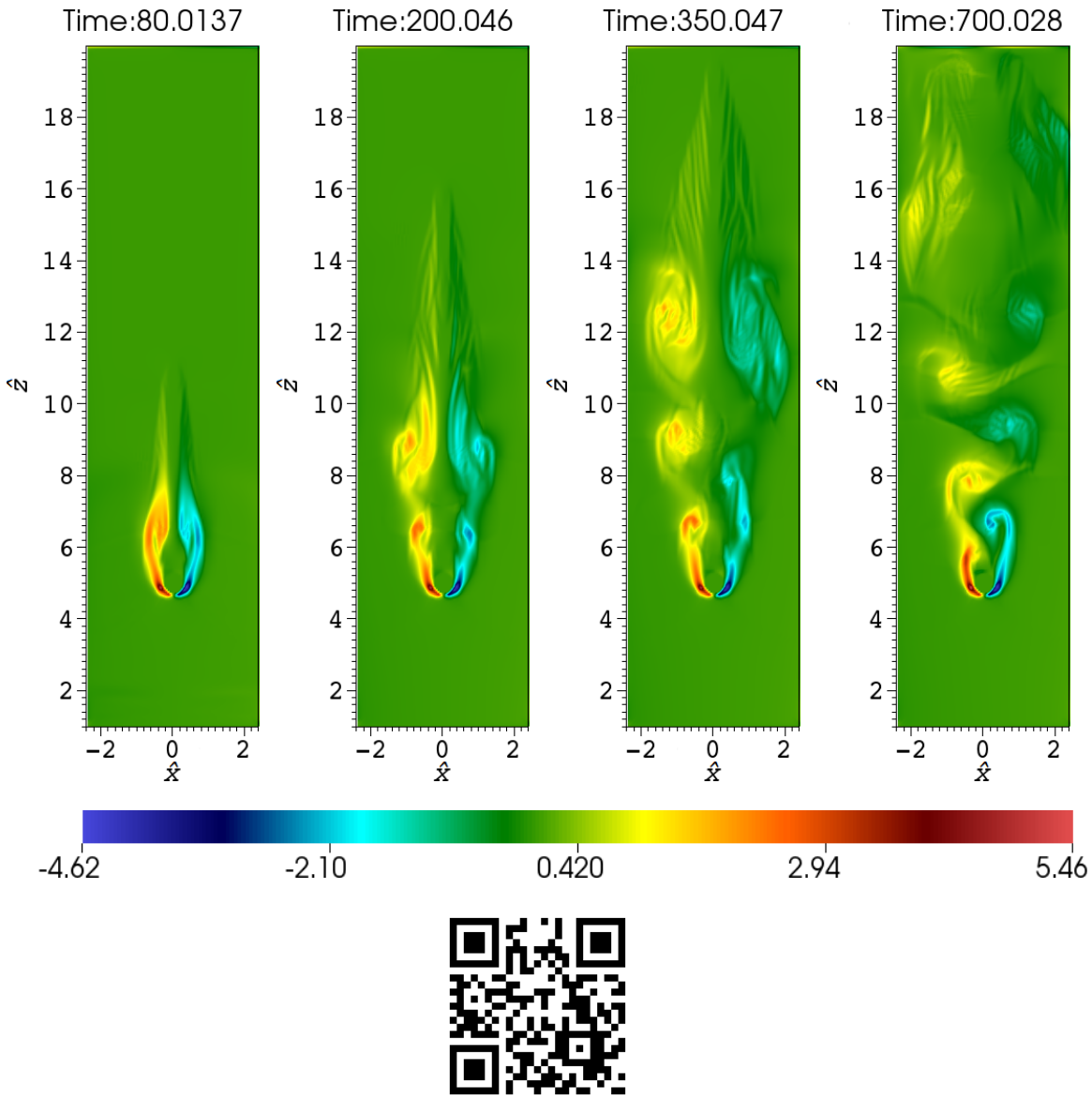

Figure 3.8: Evolution of the ω_y distribution in the units of v_{z_0}/d in the simulation with $\hat{B}_y = 0.5$. The whole process can be viewed online in the movie linked to the attached QR code.

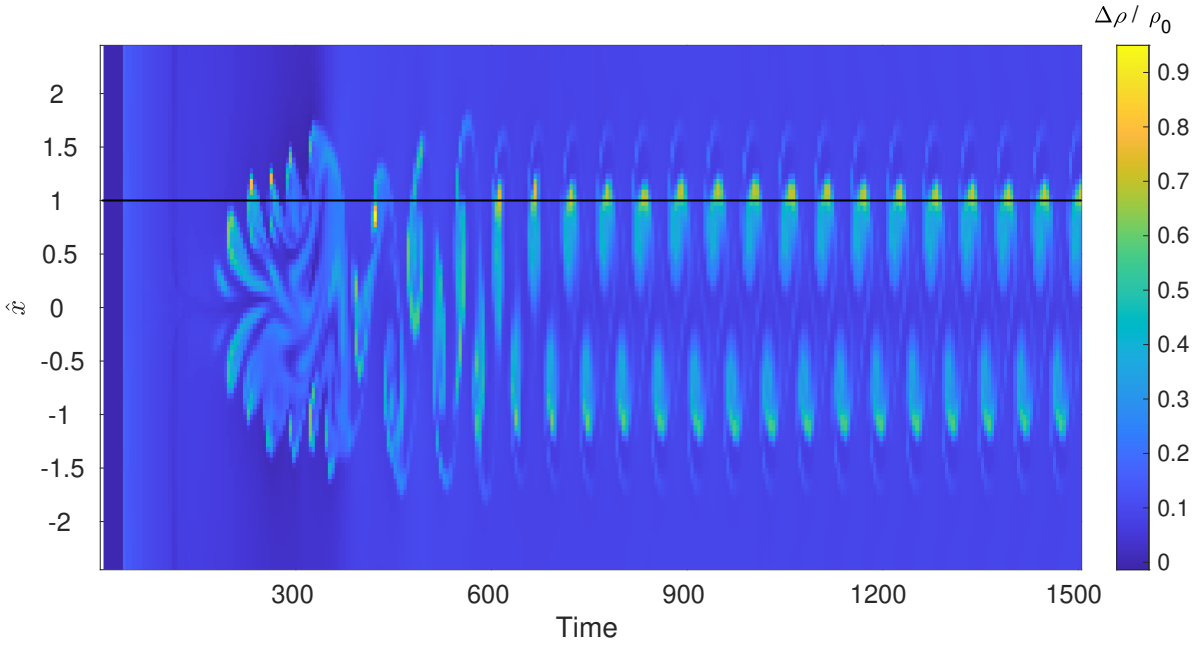

Figure 3.9: Evolution of $\Delta\rho/\rho_0$ along axis x at $\hat{y}=0$, $\hat{z}=9$ in the simulation with $\hat{B}_y=0.1$. The black line indicates the x position to which Fig. 3.10 refers.

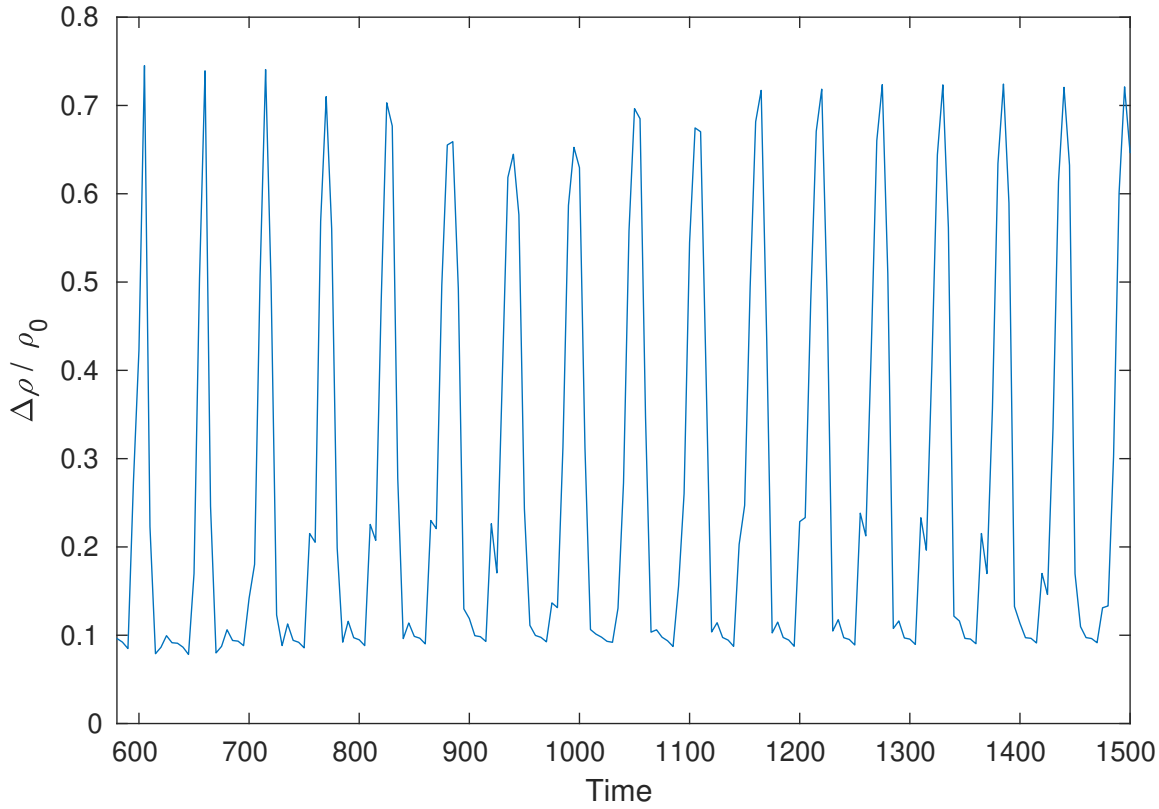

Figure 3.10: Evolution of $\Delta\rho/\rho_0$ at $\hat{x}=1$, $\hat{y}=0$, $\hat{z}=9$ in the simulation with $\hat{B}_y=0.1$. The range that was used to calculate St is displayed.

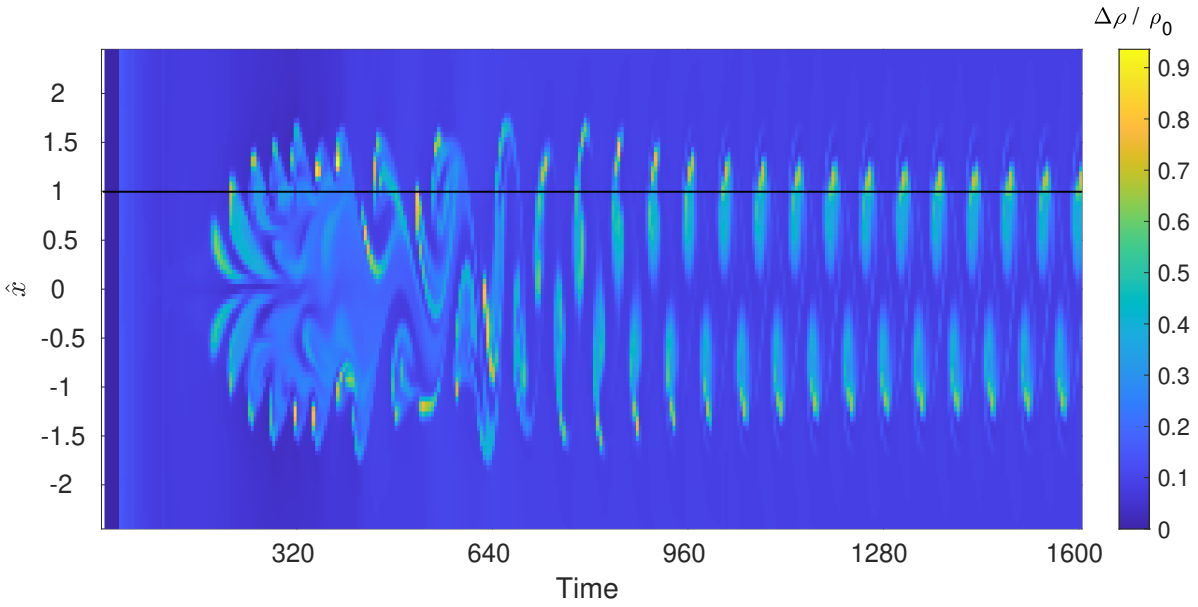

Figure 3.11: Evolution of $\Delta\rho/\rho_0$ along axis x at $\hat{y}=0$, $\hat{z}=9$ in the simulation with $\hat{B}_y=0.2$. The black line indicates the x position to which Fig. 3.12 refers.

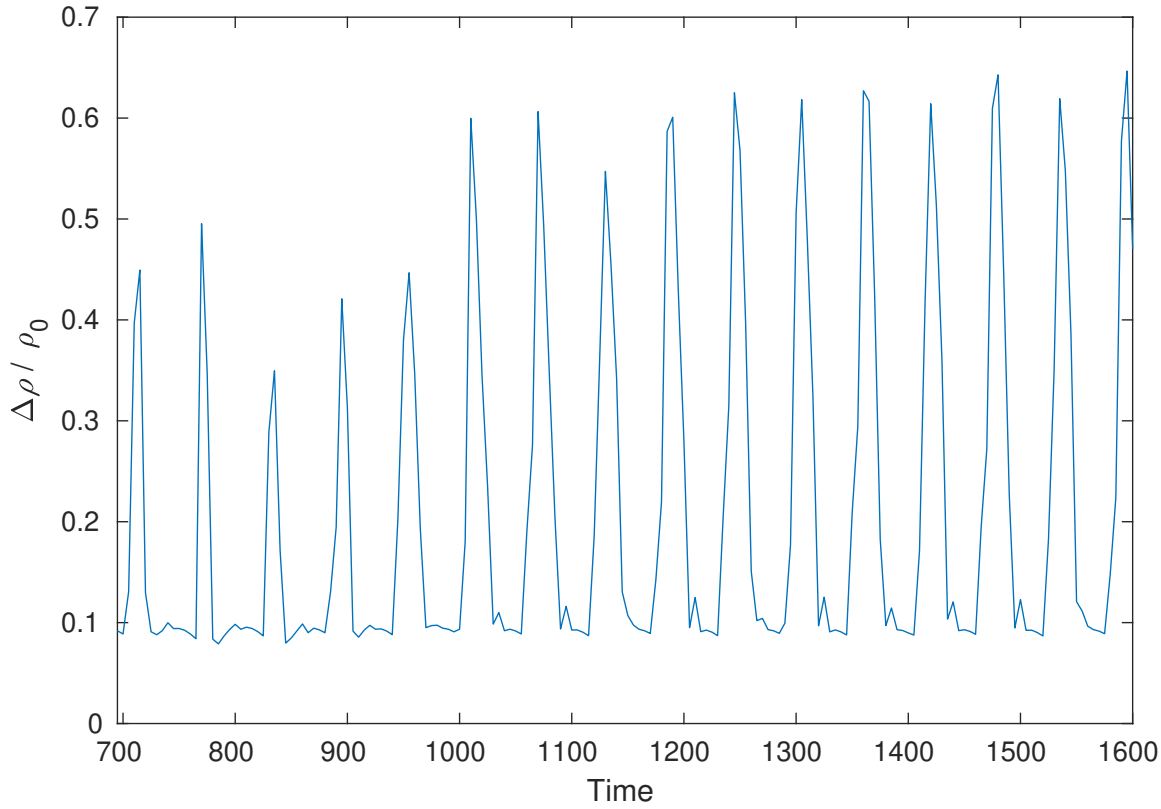

Figure 3.12: Evolution of $\Delta\rho/\rho_0$ at $\hat{x}=1$, $\hat{y}=0$, $\hat{z}=9$ in the simulation with $\hat{B}_y=0.2$. The range that was used to calculate St is displayed.

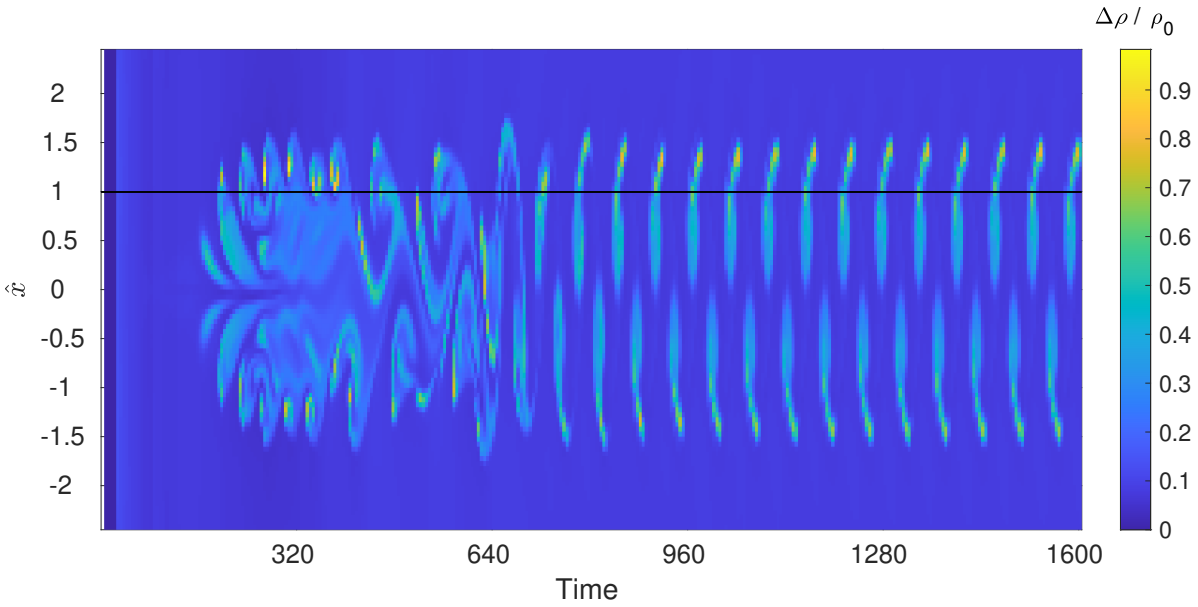

Figure 3.13: Evolution of $\Delta\rho/\rho_0$ along axis x at $\hat{y}=0$, $\hat{z}=9$ in the simulation with $\hat{B}_y=0.3$. The black line indicates the x position to which Fig. 3.14 refers.

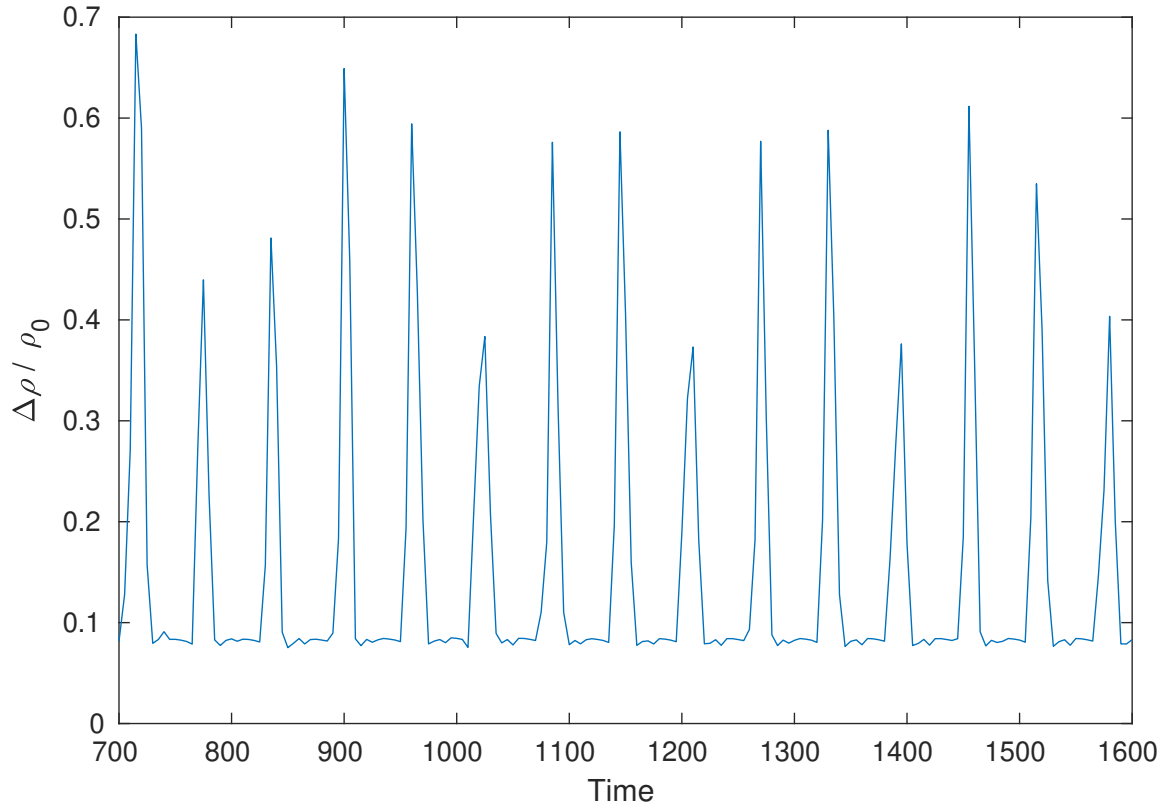

Figure 3.14: Evolution of $\Delta\rho/\rho_0$ at $\hat{x}=1$, $\hat{y}=0$, $\hat{z}=9$ in the simulation with $\hat{B}_y=0.3$. The range that was used to calculate St is displayed.

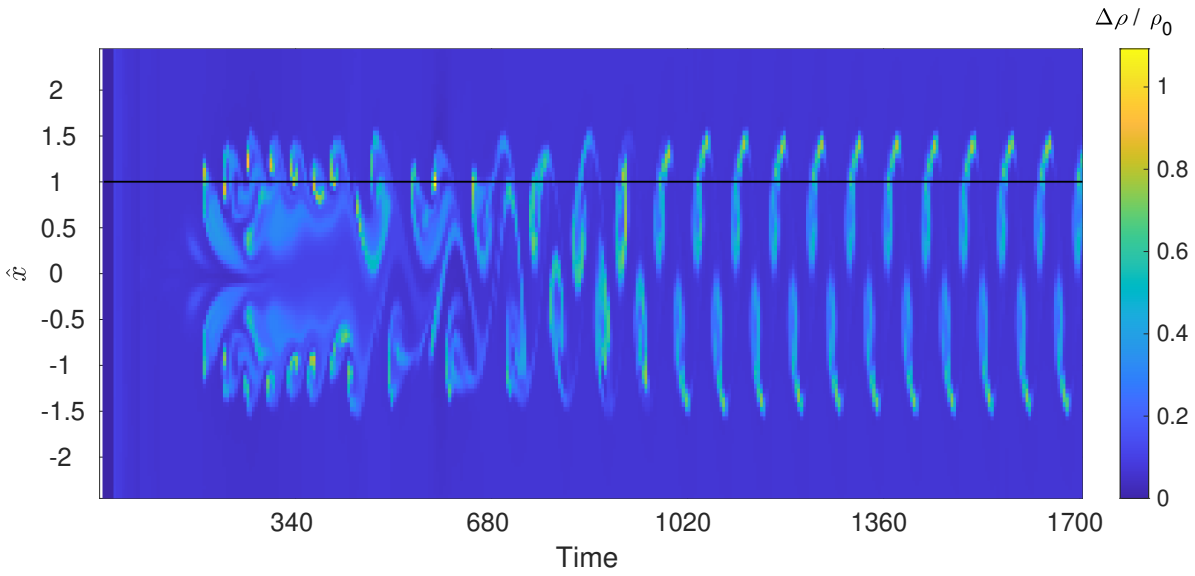

Figure 3.15: Evolution of $\Delta\rho/\rho_0$ along axis x at $\hat{y}=0$, $\hat{z}=9$ in the simulation with $\hat{B}_y=0.4$. The black line indicates the x position to which Fig. 3.16 refers.

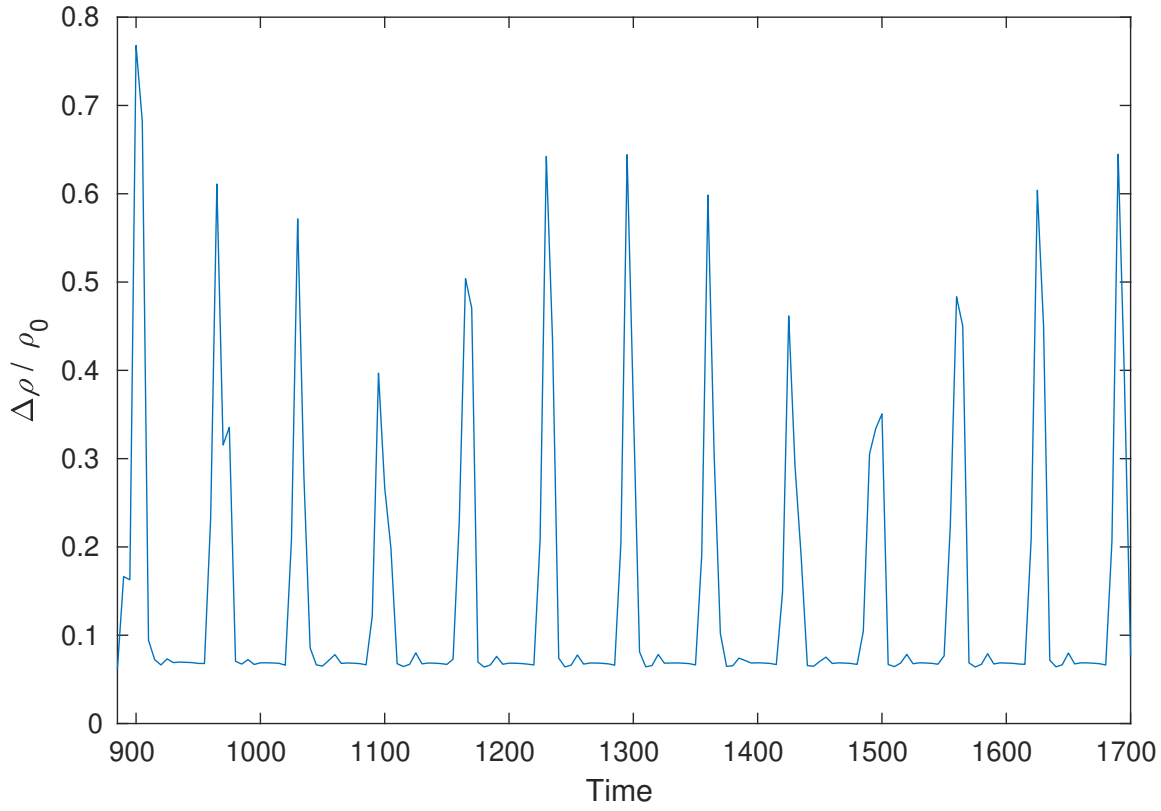

Figure 3.16: Evolution of $\Delta\rho/\rho_0$ at $\hat{x}=1$, $\hat{y}=0$, $\hat{z}=9$ in the simulation with $\hat{B}_y=0.4$. The range that was used to calculate St is displayed.

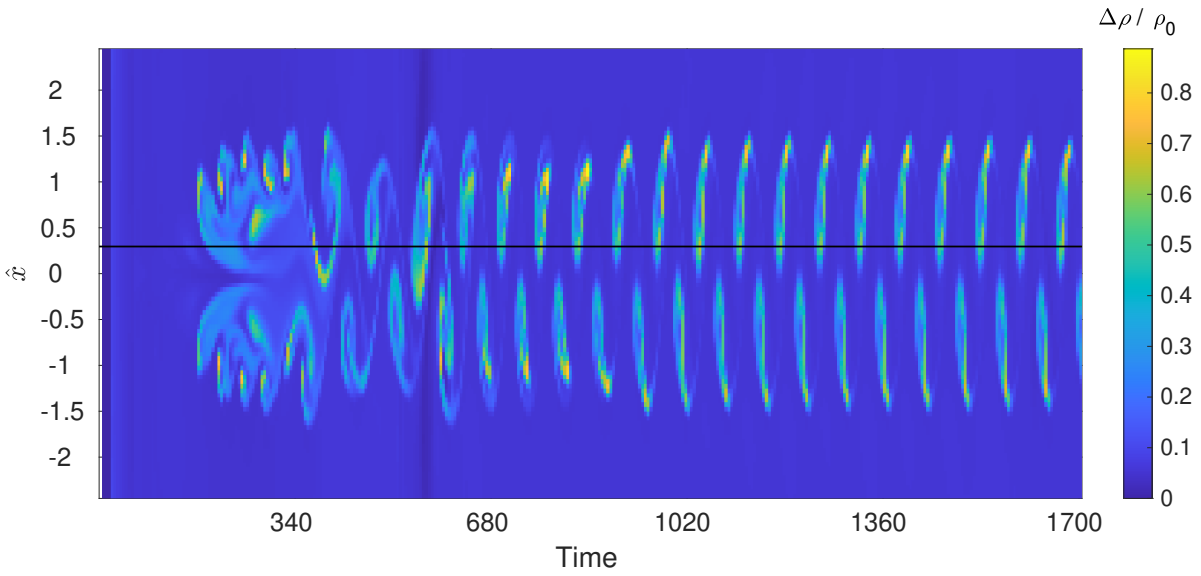

Figure 3.17: Evolution of $\Delta\rho/\rho_0$ along axis x at $\hat{y}=0$, $\hat{z}=9$ in the simulation with $\hat{B}_y=0.5$. The black line indicates the x position to which Fig. 3.18 refers.

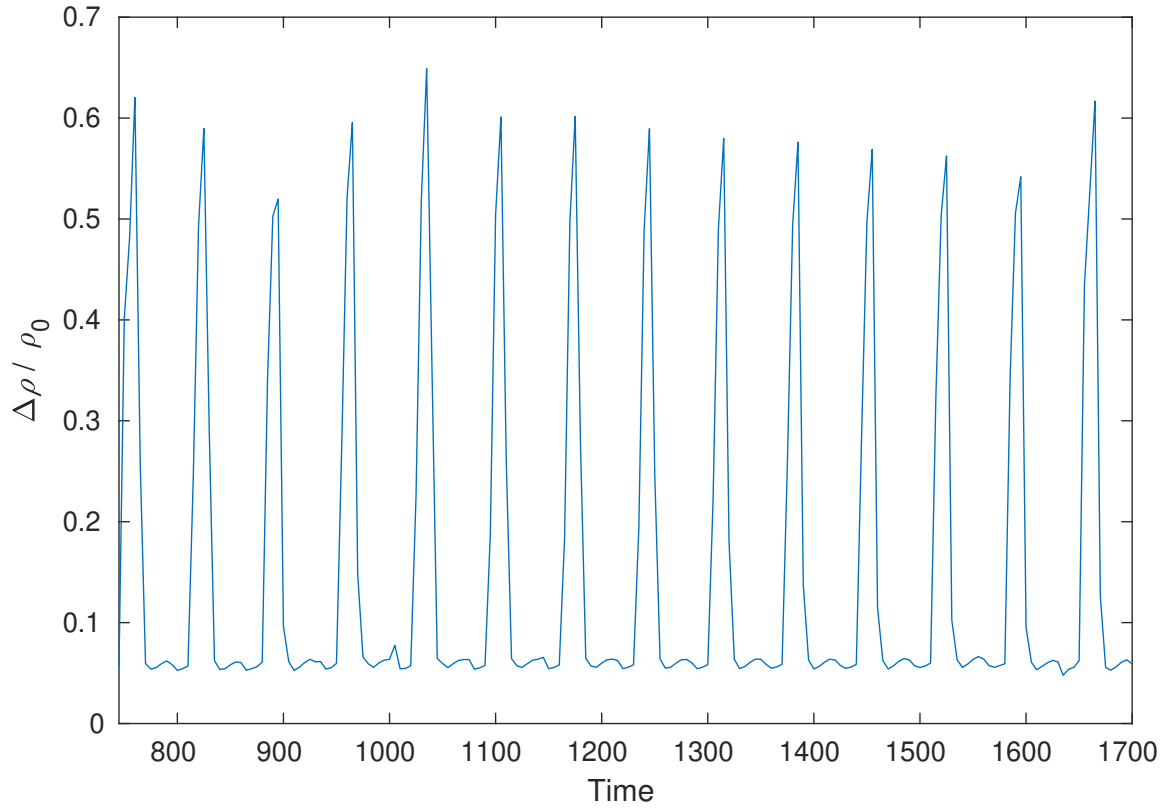

Figure 3.18: Evolution of $\Delta\rho/\rho_0$ at $\hat{x}=0.3$, $\hat{y}=0$, $\hat{z}=9$ in the simulation with $\hat{B}_y=0.5$. The range that was used to calculate St is displayed.

Table 3.2: The obtained values of vortex shedding period, flow velocity and Strouhal number from the simulations with a constant initial magnetic field

$\hat{B}_y$	$\hat{P}$	$\hat{v}$	St
0.1	55.67	0.0590	0.1926
0.2	58.44	0.0576	0.1878
0.3	61.34	0.0560	0.1841
0.4	65.75	0.0548	0.1755
0.5	69.49	0.0534	0.1704

The period value obtained from the $\Delta\rho/\rho_0$ evolution, the average flow velocity value obtained as described in Sec. 3.2.3 and the Strouhal number value calculated for each simulation are summarized in Tab. 3.2.

3.5 Dependence of the Strouhal number on the magnetic field

The dependence of the vortex shedding period and Strouhal number on the initial magnetic field in the simulations described in Secs. 3.3 and 3.4 is plotted in Fig. 3.19 in the left and right panels, respectively. The period appears to increase linearly, while the Strouhal number decreases.

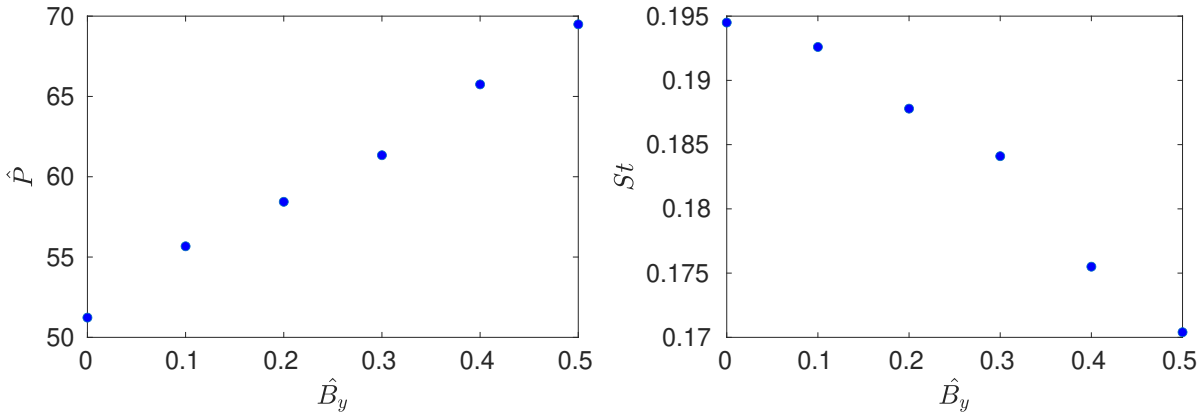

Figure 3.19: The vortex shedding period and Strouhal number vs. the initial magnetic field.

It can be stated that the increasing density of magnetic field lines perpendicular to the flow plane interferes with the flow and vortex formation and therefore leads to an increase in the vortex shedding period and a slight decrease in the flow velocity, which means a Strouhal number reduction.

3.6 Simulation with $B_\mathrm{i} > B_\mathrm{e}$ in a gravitationally stratified solar atmosphere

Figure 3.20 shows the distribution of ω_y at the same four time steps as were shown for the simulations with a gravity-free medium. Two symmetrical vortices can be seen in the first graph. A structured chain of vortices, i.e. Kármán vortex street, can be seen in the last two graphs. This shows that compared to the simulation with the same B_{y_e} (see Fig. 3.4), the vortex shedding process in this simulation begins earlier. Also, the vortices acquire higher vorticity values, but no significant difference in the structure of the vortices or their pattern can be seen.

Figure 3.21 shows the evolution of the relative density change $\Delta\rho/\rho_0$ along axis x at $\hat{y} = 0$, $\hat{z} = 9$ in this simulation. In Fig. 3.22 are plotted the data for $\hat{x} = 0.9$ in the range that was used to calculate St.

The period value obtained from the evolution of $\Delta\rho/\rho_0$, the average flow speed value obtained as described in Sec. 3.2.3 and the Strouhal number calculated are summarized in Tab. 3.3, where the results from the simulation with the same B_{y_e} without a gravitational filed are included for comparison. A slight decrease in $\hat{P}$ can be seen. The value of $\hat{v}$ is higher, even than the value obtained from the simulation with a zero magnetic field. This led to a decrease in the Strouhal number.

Table 3.3: The obtained values of vortex shedding period, flow velocity and Strouhal number from the simulations with $\hat{B}_{y_\mathrm{e}} = 0.1$ in a gravity-free and gravity medium.

	$\hat{P}$	$\hat{v}$	St
Gravity-free medium	55.67	0.0590	0.1926
Gravity medium	54.46	0.0641	0.1811

The decrease in the vortex shedding period was probably caused by the fact that the initial mass density above the cylinder centre was lower than in the simulation with a gravity-free medium due to the mass density stratification, which allowed an easier formation of vortices.

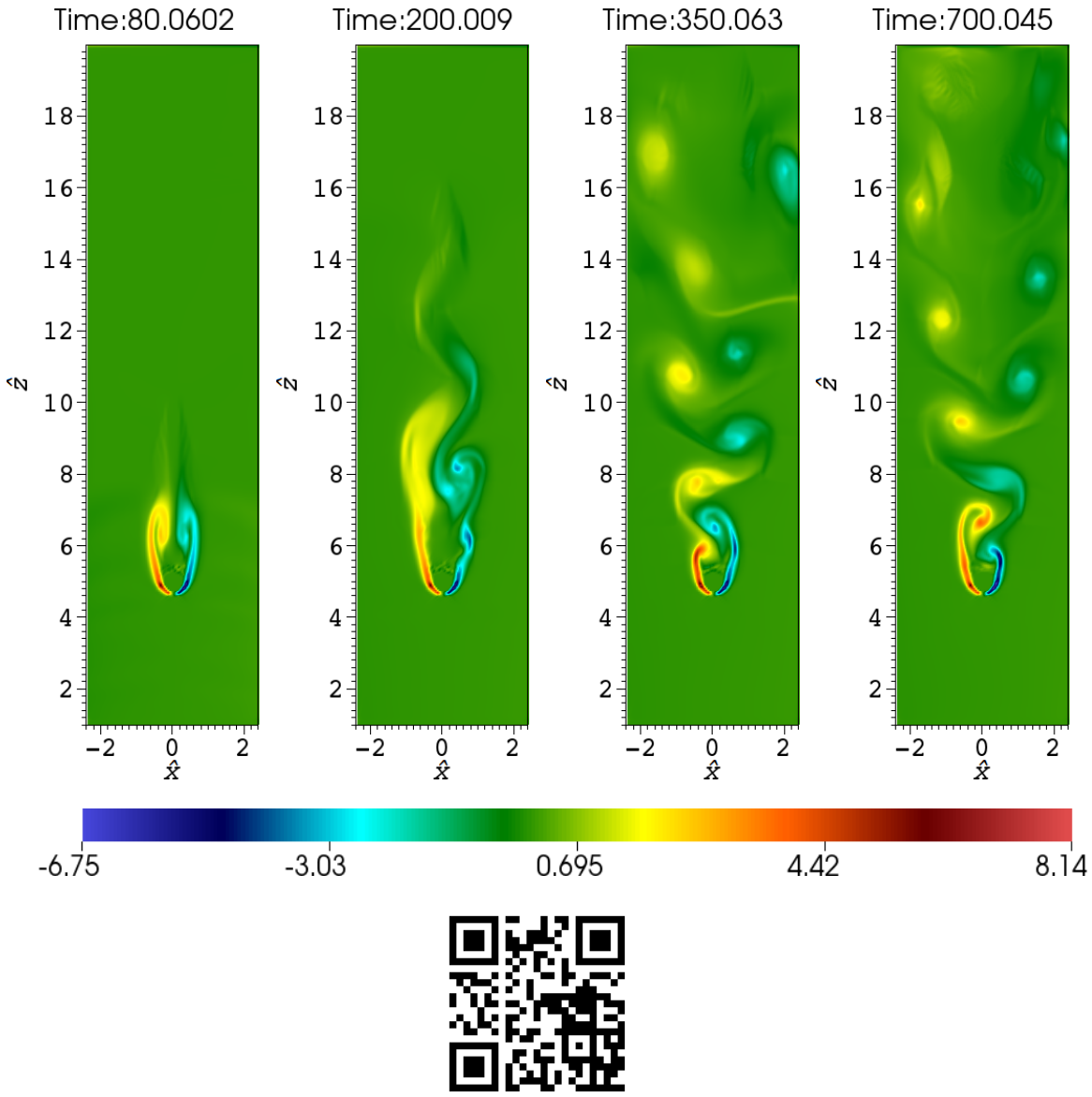

Figure 3.20: Evolution of the ω_y distribution in the units of v_{z_0}/d in the simulation in a gravitationally stratified solar atmosphere. The whole process can be viewed online in the movie linked to the attached QR code.

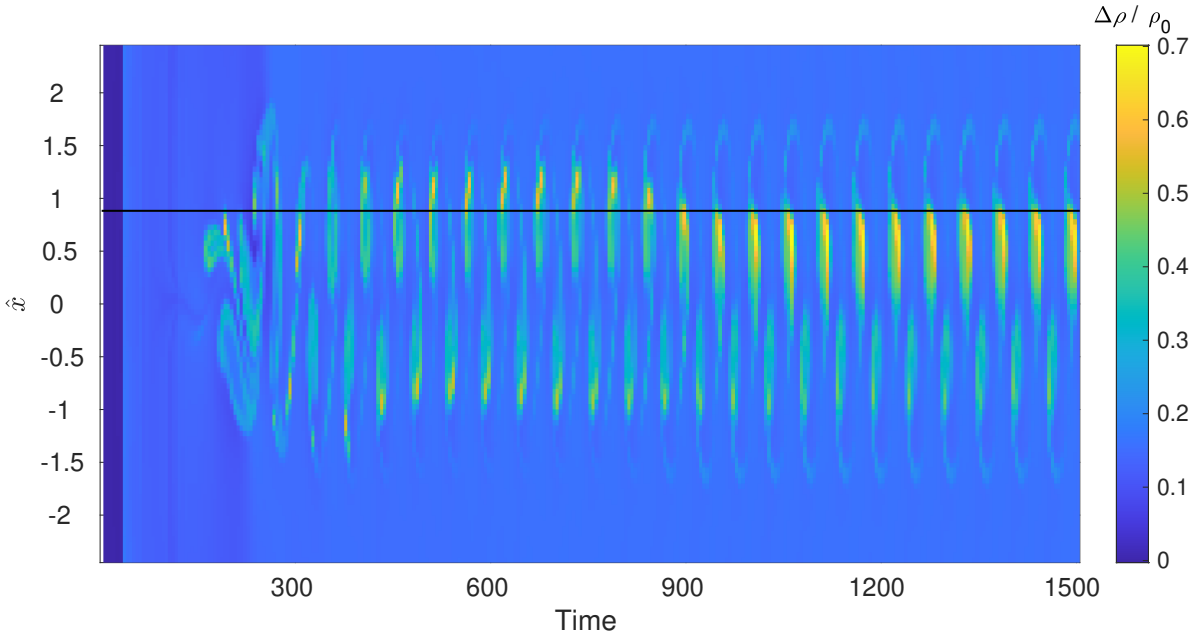

Figure 3.21: Evolution of $\Delta\rho/\rho_0$ along axis x at $\hat{y} = 0$, $\hat{z} = 9$ in the simulation in a gravitationally stratified solar atmosphere. The black line indicates the x position to which Fig. 3.22 refers.

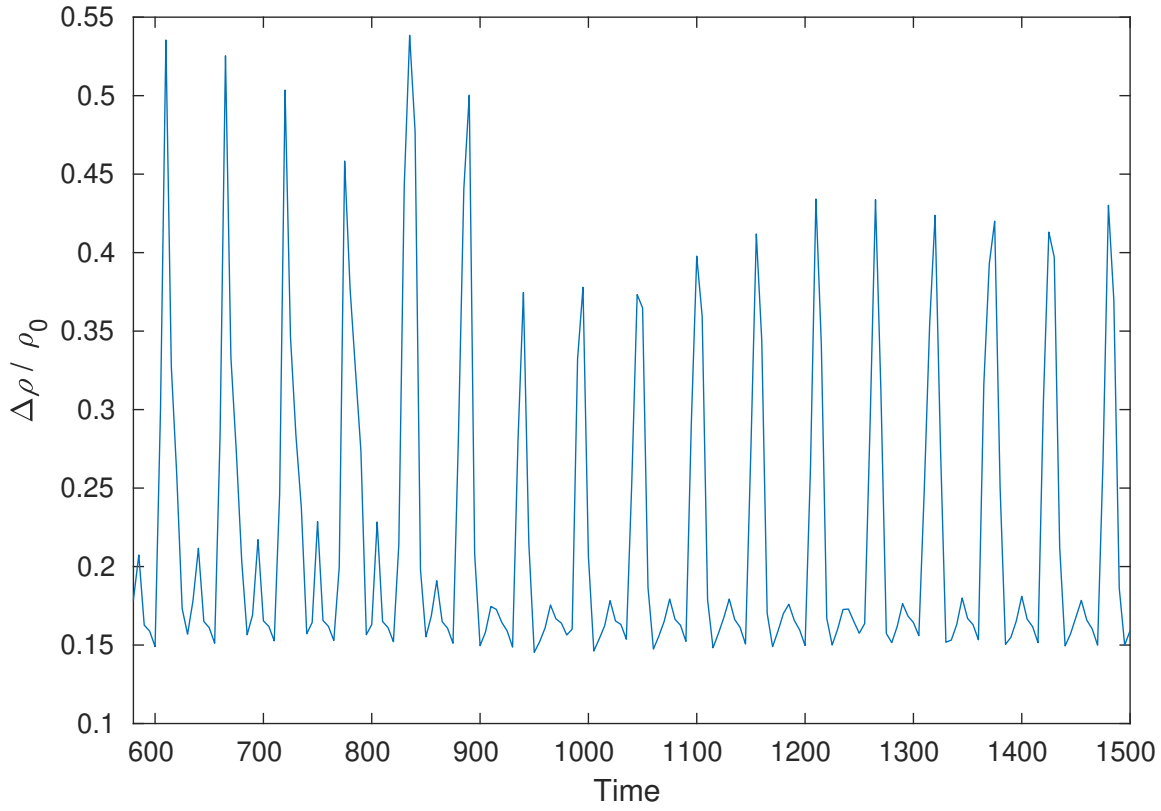

Figure 3.22: Evolution of $\Delta\rho/\rho_0$ at $\hat{x} = 0.9$, $\hat{y} = 0$, $\hat{z} = 9$ in the simulation in a gravitationally stratified solar atmosphere. The range that was used to calculate St is displayed.

4 Conclusions

The vortex shedding phenomenon was studied by numerical simulations of flow around a cylindrical body in hydrodynamic conditions and five MHD environments with different initial magnetic fields constant throughout the simulation box, including the cylinder. The parametric study performed using these simulations allowed us to evaluate the effect of the magnetic field on the vortex shedding frequency and Strouhal number. Furthermore, this phenomenon was numerically studied in an MHD environment with the solar gravitational field applied, including the mass density stratification and a cylindrical body with a magnetic field stronger than the external magnetic field, which was more consistent with the real coronal environment and magnetic structures.

Although the Strouhal number in MHD conditions has been observed in several studies, its dependence on the magnetic field has not been properly studied. In this thesis, the Strouhal number was for the first time parametrically studied in a magnetic field environment in 3D under conditions similar to those in the solar corona. This parametric study showed that increasing the initial magnetic field perpendicular to the flow plane led to a delay in the vortex shedding and a decrease in its frequency and the Strouhal number. It also caused changes in the structure of the vortices – they were larger and acquired lower vorticity values. The Strouhal number was each time close to the value of 0.2, which is typically stated as the usual approximate Strouhal number value of vortex shedding.

The application of a solar gravitational field, including the environment mass density stratification and a stronger magnetic field inside the cylindrical body, showed that the vortex shedding process in these conditions occurs in a fashion similar to the gravity-free case with the same initial external magnetic field, which was constant throughout the whole simulation box, in-

cluding the cylinder. However, it led to a slight increase in the frequency of vortex shedding, which began at an earlier time, and a slight decrease in the Strouhal number.

Preliminary results of this thesis were presented at the 16th European Solar Physics Meeting[1] by a poster contribution – see documentation in the Appendix.

Further work could include modifying the model by applying a fixed but non-rigid cylindrical body to perform numerical simulations of oscillations in magnetic structures, where the zero velocity condition would be kept only in the cylinder bases. Due to the deformation of the cylindrical body by the fluid flow, it would be problematic to apply fixed values inside it. Therefore, to avoid destructive deformation, which was happening in our past attempts, the velocity boundary condition determining the flow could be maintained for a limited time. Also, multiple cylindrical bodies, which would represent prominence threads, could be applied.

All data obtained by numerical simulations within the solution of this master's thesis are stored at the Department of Physics, Faculty of Science, University of South Bohemia in České Budějovice. The calculations were performed on the computer Dell T3600; Intel© Xeon© CPU E5-1650 0, 3.20 GHz $\times$ 6. The work was supported by the international CZ-RU bilateral project 21-16508J of the Grant Agency of the Czech Republic.

[1] `https://indico.ict.inaf.it/event/794/`

List of figures

List of tables

Bibliography

[1] ANDRETTA, V. et al. The first coronal mass ejection observed in both visible-light and UV H I Ly-α channels of the Metis coronagraph on board Solar Orbiter. *Astronomy & Astrophysics*. 2021, **656**, L14. ISSN 1432-0746.

[2] ANTIA, H. M., BHATNAGAR, A. and ULMSCHNEIDER, P. (eds.). *Lectures on Solar Physics*. Springer-Verlag Berlin Heidelberg, 2003. ISBN 978-3-540-01528-4.

[3] ARBER, Tony. *LareXd User Guide* [online]. Coventry: University of Warwick, 2020 [cit. 07.04.2022]. Available at `https://warwick.ac.uk/fac/sci/physics/research/cfsa/people/tda/larexd/larexd-manual.pdf`

[4] ARREGUI, Iñigo, OLIVER, Ramón and BALLESTER, José Luis. Prominence oscillations. *Living Reviews in Solar Physics*. 2018, **15**, 3. ISSN 1614-4961.

[5] ASCHWANDEN, Markus J. *Physics of the Solar Corona: An Introduction with Problems and Solutions*. Springer-Verlag Berlin Heidelberg New York, 2006. ISBN 3-540-30765-6.

[6] AVRETT, Eugene H. and LOESER, Rudolf. Models of the Solar Chromosphere and Transition Region from SUMER and HRTS Observations: Formation of the Extreme-Ultraviolet Spectrum of Hydrogen, Carbon, and Oxygen. *The Astrophysical Journal Supplement Series*. 2008, **175**(1), 229. ISSN 1538-4365.

[7] BALLESTER, J. L., CARBONELL, M., SOLER, R. and TERRADAS, J. Prominence oscillations: Effect of a time-dependent background temperature. *Astronomy & Astrophysics*. 2016, **591**, A109. ISSN 1432-0746.

[8] BELOV, Sofya. *Proudění tekutiny v okolí překážky kruhového průřezu*. České Budějovice, 2020. Bachelor thesis. University of South Bohemia in České Budějovice. Faculty of Science. Institute of Physics.

[9] CHIUDERI, Claudio and VELLI, Marco. *Basics of Plasma Astrophysics*. Springer-Verlag Italia, 2015. ISBN 978-88-470-5870-5.

[10] CHUNG, T. J. *Computational Fluid Dynamics*. Cambridge: Cambridge University Press, 2002. ISBN 0-521-59416-2.

[11] CRANMER, Steven R. and WINEBARGER, Amy R. The Properties of the Solar Corona and Its Connection to the Solar Wind. *Annual Review of Astronomy and Astrophysics*. 2019, **57**, 157–187. ISSN 1545-4282.

[12] DOUSSET, Vincent and POTHÉRAT, Alban. Numerical simulations of a cylinder wake under a strong axial magnetic field. *Physics of Fluids*. 2018, **20**(1), 017104. ISSN 1089-7666.

[13] DRUCKMÜLLER, Miloslav. *Total Solar Eclipse 2019 image, Corona up to 5 solar radii* [online]. Brno: Brno University of Technology, 2019 [cit 06.04.2022]. Available at `http://www.zam.fme.vutbr.cz/~druck/Eclipse/Ecl2019ch/Tres_Cruses/TC_347mm/0-info.htm`

[14] DYNNIKOVA, G. Ya., DYNNIKOV, Ya. A. and GUVERNYUK, S. V. Mechanism underlying Kármán vortex street breakdown preceding secondary vortex street. *Physics of Fluids*. 2016, **28**(5), 054101. ISSN 1089-7666.

[15] ENGVOLD, Oddbjørn, VIAL, Jean-Claude and SKUMANICH, Andrew (eds.). *The sun as a guide to stellar physics*. Amsterdam: Elsevier, 2019. ISBN 978-0-12-814334-6.

[16] FARGE, Marie. Wavelet Transforms and their Applications to Turbulence. *Annual Review of Fluid Mechanics*. 1992, **24**, 395–457, 1992. ISSN 1545-4479.

[17] FOUKAL, Peter V. *Solar Astrophysics*. 2nd ed. Weinheim: Wiley-VCH Verlag, 2013. ISBN 3-527-40374-4.

[18] GOEDBLOED, J. P. Hans and POEDTS, Stefaan. *Principles of Magnetohydrodynamics*. Cambridge: Cambridge University Press, 2004. ISBN 0-521-62607-2.

[19] GONZÁLEZ, José Juan, GUZMÁN, F. S., FEDUN, V., VERTH, Gary, SHEYLAG, Sergiy and REGNIER, Stephane. I. Jet Formation and Evolution Due to 3D Magnetic Reconnection. *The Astrophysical Journal*. 2018, **856**(176), 1538. ISSN 1538-4357.

[20] GREEN, Lucie M., TÖRÖK, Tibor, VRŠNAK, Bojan, MANCHESTER, Ward and VERONIG, Astrid. The Origin, Early Evolution and Predictability of Solar Eruptions. *Space Science Reviews*. 2018, **214**(1), 46. ISSN 1572-9672.

[21] GRIFFIES, Stephen, ADCROFT, Alistair and HALLBERG, Robert W. A Primer on the Vertical Lagrangian-Remap Method in Ocean Models Based on Finite Volume Generalized Vertical Coordinates. *Journal of Advances in Modeling Earth Systems*. 2020, **12**(10). ISSN 1942-2466.

[22] GRUSZECKI, M., NAKARIAKOV, V. M., VAN DOORSSELAERE, T. and ARBER, T. D. Phenomenon of Alfvénic Vortex Shedding. *Physical Review Letters*. 2010, **105**(5), 055004. ISSN 1079-7114.

[23] JELÍNEK, Petr. *Magnetohydrodynamické vlny a oscilace ve sluneční koróně*. České Budějovice: University of South Bohemia in České Budějovice, Faculty of Science, 2017. ISBN 978-80-7394-656-2.

[24] JESS, D. B., MORTON, R. J., VERTH, G., FEDUN, V., S. D. T. Grant and GIAGKIOZIS, I. Multiwavelength Studies of MHD Waves in the Solar Chromosphere. *Space Science Reviews*. 2015, **190**(1-4), 103–161. ISSN 0038-6308.

[25] HUDSON, H. S. and WARMUTH, A. Coronal loop oscillations and flare shock waves. *The Astrophysical Journal*. 2008, **614**, L85–L88. ISSN 1538-4357.

[26] KARAMPELAS, Konstantinos and VAN DOORSSELAERE, Tom. Transverse Loop Oscillations via Vortex Shedding: A Self-oscillating Process. *The Astrophysical Journal Letters*. 2021, **908**(1), L7. ISSN 2041-8213.

[27] KASPER, J. C. et al. *Parker Solar Probe* Enters the Magnetically Dominated Solar Corona. *Physical Review Letters*. 2021, **127**, 255101. ISSN 1079-7114.

[28] LANG, Kenneth R. *Essential astrophysics*. Springer-Verlag Berlin Heidelberg, 2013. ISBN 978-3-642-35963-7.

[29] LEE, Harim, MOON, Y.-J. and NAKARIAKOV, V. M. Radial and Azimuthal Oscillations in Halo Coronal Mass Ejections in the Sun. *The Astrophysical Journal Letters*. 2015, **803**(1), L7. ISSN 2041-8213.

[30] MEYERS, Robert A. (ed.). *Encyclopedia of Physical Science and Technology*. 3rd ed. San Diego: Academic Press, 2001. ISBN 978-0-12-227410-7.

[31] NAKARIAKOV, V. M., ASCHWANDEN, M. J. and VAN DOORSSELAERE, T. The possible role of vortex shedding in the excitation of kink-mode oscillations in the solar corona. *Astronomy & Astrophysics*. 2009, **502**(2), 661–664. ISSN 1432-0746.

[32] NAKARIAKOV, V. M. and VERWICHTE, E. Coronal Waves and Oscillations. *Living Reviews in Solar Physics*. 2005, **2**, 3. ISSN 1614-4961.

[33] NASA. *Catalog Page for PIA03149* [online]. 2001 [cit. 15.03.2022]. Available at `https://photojournal.jpl.nasa.gov/catalog/PIA03149`

[34] PRIEST, Eric. *Magnetohydrodynamics of the Sun*. New York: Cambridge University Press, 2014. ISBN 978-0-521-85471-9.

[35] SAMANTA, Tanmoy, TIAN, Hui and NAKARIAKOV, Valery M. Evidence for Vortex Shedding in the Sun's Hot Corona. *Physical Review Letters*. 2019, **123**(3), 035102. ISSN 1079-7114.

[36] SINGHA, Sintu, SINHAMAHAPATRA, K. P. and MUKHERJEA, S. K. Control of Vortex Shedding From a Bluff Body Using Imposed Magnetic Field. *Journal of Fluids Engineering*. 2007, **129**(5), 517–523. ISSN 1528-901X.

[37] SPOHN, Tilman, BREUER, Doris and JOHNSON, Torrence V. (eds.). *Encyclopedia of the Solar System*. 3rd ed. Amsterdam: Elsevier, 2014. ISBN 978-0-12-415845-0.

[38] TORRENCE, Christopher and COMPO, Gilbert P. A Practical Guide to Wavelet Analysis. *Bulletin of the American Meteorological Society*. 1998, **79**(1), 61–78, 1998. ISSN 1520-0477.

[39] TRIPATHI, D., ISOBE, H. and JAIN, R. Large amplitude oscillations in prominences. *Space Science Reviews*. 2019, **149**, 283–298. ISSN 0038-6308.

[40] VERWICHTE, Erwin. *Visualisation of linear MHD waves in a coronal loop* [online]. Coventry: University of Warwick, 2013 [cit. 18.03.2022]. Available at https://warwick.ac.uk/fac/sci/physics/research/cfsa/research/wpc/vis/?fbclid=IwAR2TZpnpxVNwdn4TBgwzDi6pbIZIY-KKSHcjHWMiO4uSI4kMXGO1oPGr6rI

[41] WANG, H. N. and XU, R. L. (eds.). *Solar-Terrestrial Magnetic Activity and Space Environment*. Pergamon, 2002. ISBN 978-0-08-044110-8.

[42] WHITE, Frank M. *Viscous Fluid Flow*. 3rd ed. New York: McGraw-Hill, 2006. ISBN 007-124493-X.

[43] YADAV, V. K. Plasma Waves in the Sun. *Universal Journal of Physics and Application*. 2016, **10**(6), 193–197. ISSN 2331-6535.

[44] ZIMOVETS, I. V. and NAKARIAKOV, V. M. Excitation of kink oscillations of coronal loops: statistical study. *Astronomy & Astrophysics*. 2015, **577**, A4. ISSN 1432-0746.

Appendix

16th European Solar Physics Meeting

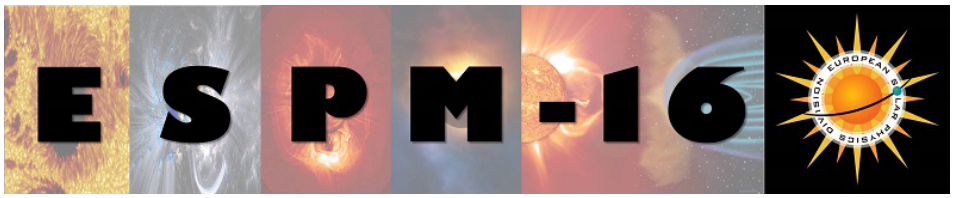

Preliminary results of this thesis were presented by a poster contribution at the 16th European Solar Meeting (ESPM-16). The European Solar Meetings are major gatherings devoted to theoretical and observational studies of solar phenomena, organised by the board of the European Solar Physics Division every three years. Initially planned for 2020, this meeting took place in 2021 on a virtual conference platform, where the poster contribution was accompanied by an oral presentation given by the author of the thesis. The abstract, poster and a screenshot from the online presentation can be seen below.

Contribution ID: **368** Type: **Poster**

Study of Alfvénic vortex shedding past a cylindrical obstacle

Tuesday, September 7, 2021 9:13 AM (13 minutes)

In this paper, the phenomenon of vortex shedding around a circular cylindrical obstacle is studied numerically in magnetohydrodynamic (MHD) conditions in three spatial dimensions using the numerical code Lare3d. A parametric study was performed for different values of magnetic field perpendicular to the plasma flow plane. This model mimics coronal mass ejection flowing around a coronal loop, which is known as a probable mechanism for excitation of kink-mode oscillations in coronal loops. The phenomenon of vortex shedding has been widely studied in hydrodynamic conditions in both science and engineering, it has also been investigated by a number of numerical simulations in magnetic field environments, mainly in two dimensions. In MHD conditions, however, it is poorly understood.

Primary authors: BELOV, Sofya (University of South Bohemia, Faculty of Science, Department of Physics); JELÍNEK, Petr (University of South Bohemia, Faculty of Science, Department of Physics)

Presenter: BELOV, Sofya (University of South Bohemia, Faculty of Science, Department of Physics)

Session Classification: Poster Session 3.3

Track Classification: Session 2 - The Solar Atmosphere: Heating, Dynamics and Coupling

Study of Alfvénic vortex shedding past a cylindrical obstacle

Sofya Belov, Petr Jelínek

University of South Bohemia, Faculty of Science, Department of Physics, Branišovská 1760, 370 05 České Budějovice, Czech Republic

e-mail: belovs00@prf.jcu.cz, pjelinek@prf.jcu.cz

Introduction

Over a wide range of Reynolds numbers, fluid flow around a bluff obstacle, such as a circular cylinder, may lead to the creation of a chain of vortices (Kármán vortex street) that form just behind the obstacle and disconnect from it periodically and alternately from each side. This periodic vortex formation is called vortex shedding [1].

This phenomenon has been widely studied in hydrodynamic conditions, but is less well understood in magnetohydrodynamic (MHD) conditions [2]. It has been investigated by a number of numerical simulations in magnetic field environments, mainly in two dimensions – e.g. [2, 3, 4].

Observations suggest the possibility of its occurrence in the Sun's atmosphere [5]. For example, radial and azimuthal oscillations that may be related to self-oscillating processes such as vortex shedding have been observed in coronal mass ejections [6]. It is also a possible mechanism for excitation of kink mode oscillations in coronal loops [7].

Numerical model

The phenomenon of vortex shedding around a circular cylindrical obstacle was studied numerically in MHD conditions in three spatial dimensions using the numerical code Lare3d. A parametric study was performed for different values of magnetic field (0, 5, 10 and 15 G) perpendicular to the plasma flow plane and the same initial flow velocity and obstacle size.

This model mimics coronal mass ejection flowing around a coronal loop and leading to vortex shedding, which is known as a probable mechanism for excitation of kink-mode oscillations in coronal loops [7].

Numerical simulations were performed using the simulation box shown in the illustration (Figure 1). Each simulation lasted $t = 1000$ in time units corresponding to about 1.12 s.

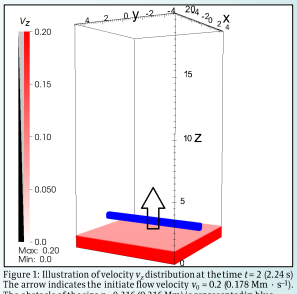

Figure 1: Illustration of velocity v_z distribution at the time $t = 2$ (2.24 s) The arrow indicates the initiate flow velocity $v_0 = 0.2$ (0.178 Mm · s^{-1}). The obstacle of the size $r = 0.316$ (0.316 Mm) is represented in blue.

The gravitational field was not considered and the ideal MHD equations were used:

$$\frac{\partial \rho}{\partial t} + \nabla \cdot \rho \mathbf{v} = 0, \tag{1}$$

$$\rho \frac{\partial \mathbf{v}}{\partial t} + \rho(\mathbf{v} \cdot \nabla)\mathbf{v} + \nabla p - \frac{1}{\mu_0}(\nabla \times \mathbf{B}) \times \mathbf{B} = 0, \tag{2}$$

$$\frac{\partial p}{\partial t} + \mathbf{v} \cdot \nabla p + \gamma p \nabla \cdot \mathbf{v} = 0, \tag{3}$$

$$\frac{\partial \mathbf{B}}{\partial t} - \nabla \times (\mathbf{v} \times \mathbf{B}) = 0, \qquad \nabla \cdot \mathbf{B} = 0, \tag{4}$$

where ρ is the fluid density, $\mathbf{v}$ is the flow rate, p is the gas pressure, $\mathbf{B}$ is the magnetic induction, μ_0 is the vacuum permeability and γ is the heat capacity ratio.

Results

Figures 2 and 3 present the density distribution at three timesteps in non-magnetic field environment and in the strongest magnetic field to copmare the time evolution of the vortex shedding process in both cases. Figure 4 presents the density distribution in all the simulations at the last timestep to compare the structure of the developped drag. Finally, Figure 5 presents the time evolution of the relative density change in all the simulations which enables to analyze the period of this proces using wavelet analysis [8].

Time evoution of density - environment without magnetic field

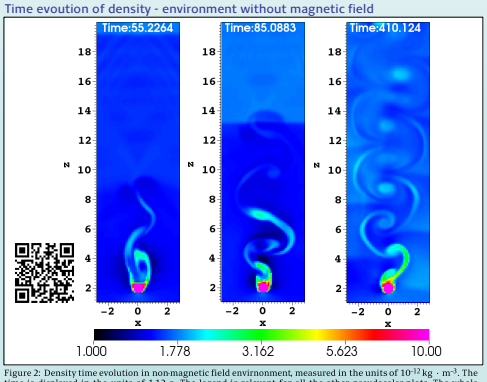

Figure 2: Density time evolution in non-magnetic field environment, measured in the units of 10^{-12} kg · m^{-3}. The time is displayed in the units of 1.12 s. The legend is relevant for all the other pseudocolor plots. The whole simulation can be viewed online in the video referenced by the QR code.

Time evolution of density - environment with magnetic field 15 G

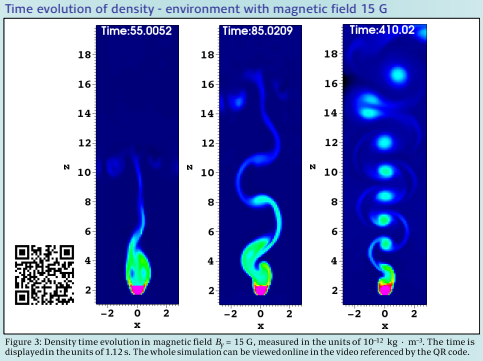

Figure 3: Density time evolution in magnetic field $B_y = 15$ G, measured in the units of 10^{-12} kg · m^{-3}. The time is displayed in the units of 1.12 s. The whole simulation can be viewed online in the video referenced by the QR code.

Density distribution – comparation

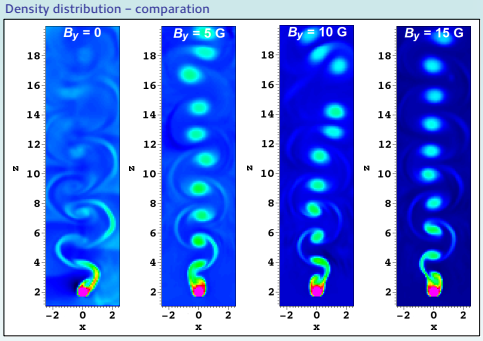

Figure 4: Density distribution at the last timestep 1000 (1120 s) for all the values of B_y, measured in the units of 10^{-12} kg · m^{-3}.

Conclusion

The process of vortex shedding and the structure of Kármán vortex street has been studied numerically in hydrodynamic environment and three different MHD environments. The simulations show that in the MHD case denser vortices are created. It is also evident that the presence of magnetic field perpendicular to the flow plane makes the vortex shedding frequency increase and causes higher periodical density changes. In the future we intend to use stronger magnetic field inside the obstacle and extend the problem on gravitational field to approximate it more to the solar corona.

Relative density change – comparation

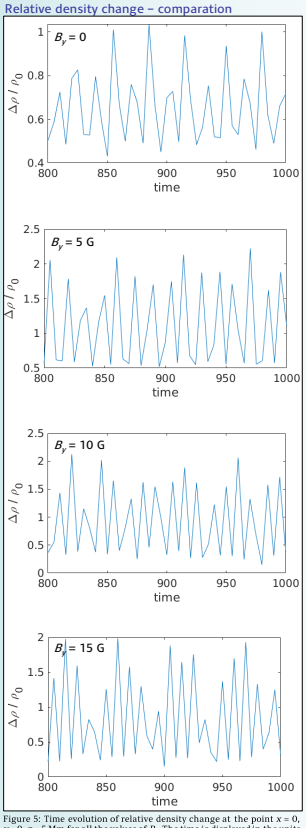

Figure 5: Time evolution of relative density change at the point $x = 0$, $y = 0$, $z = 5$ Mm for all the values of B_y. The time is displayed in the units of 1.12 s.

B_y	0	5 G	10 G	15 G
P	12.701	10.830	9.428	8.736

Table 1: Values of vortex shedding period obtained from the time evolution of relative density change using wavelet analysis [8], in the units of 1.12 s.

Acknowledgement

The authors acknowledge support from the international bilateral project 21-16508J of the Grant Agency of the Czech Republic.

[1] F. White, *Viscous fluid flow*, 3rd ed. New York: McGraw-Hill, 2006.
[2] M. Gruszecki, V. Nakariakov, T. Van Doorsselaere and T. Arber, "Phenomenon of Alfvénic Vortex Shedding", *Physical Review Letters*, vol. 105, no. 5, p. 055004, 2010.
[3] V. Dousset and A. Pothérat, "Numerical simulations of a cylinder wake under a strong axial magnetic field", *Physics of Fluids*, vol. 20, no. 1, p. 017104, 2008.
[4] S. Singha, K. Sinhamahapatra and S. Mukherjea, "Control of Vortex Shedding From a Bluff Body Using Imposed Magnetic Field", *Journal of Fluids Engineering*, vol. 129, no. 5, pp. 517-523, 2006.
[5] T. Samanta, H. Tian and V. Nakariakov, "Evidence for Vortex Shedding in the Sun's Hot Corona", *Physical Review Letters*, vol. 123, no. 3, 2019.
[6] H. Lee, Y. Moon and V. Nakariakov, "Radial and Azimuthal Oscillations in Halo Coronal Mass Ejections in the Sun", *The Astrophysical Journal Letters*, vol. 803, no. 1, p. L7, 2015.
[7] V. Nakariakov, M. Aschwanden and T. Van Doorsselaere, "The possible role of vortex shedding in the excitation of kink-mode oscillations in the solar corona", *Astronomy & Astrophysics*, vol. 502, no. 2, pp. 661-664, 2009.
[8] C. Torrence and G. P. Compo. "A Practical Guide to Wavelet Analysis", *Bulletin of the American Meteorological Society*, vol. 79, pp. 61-78, 1998.

Zoom Meeting

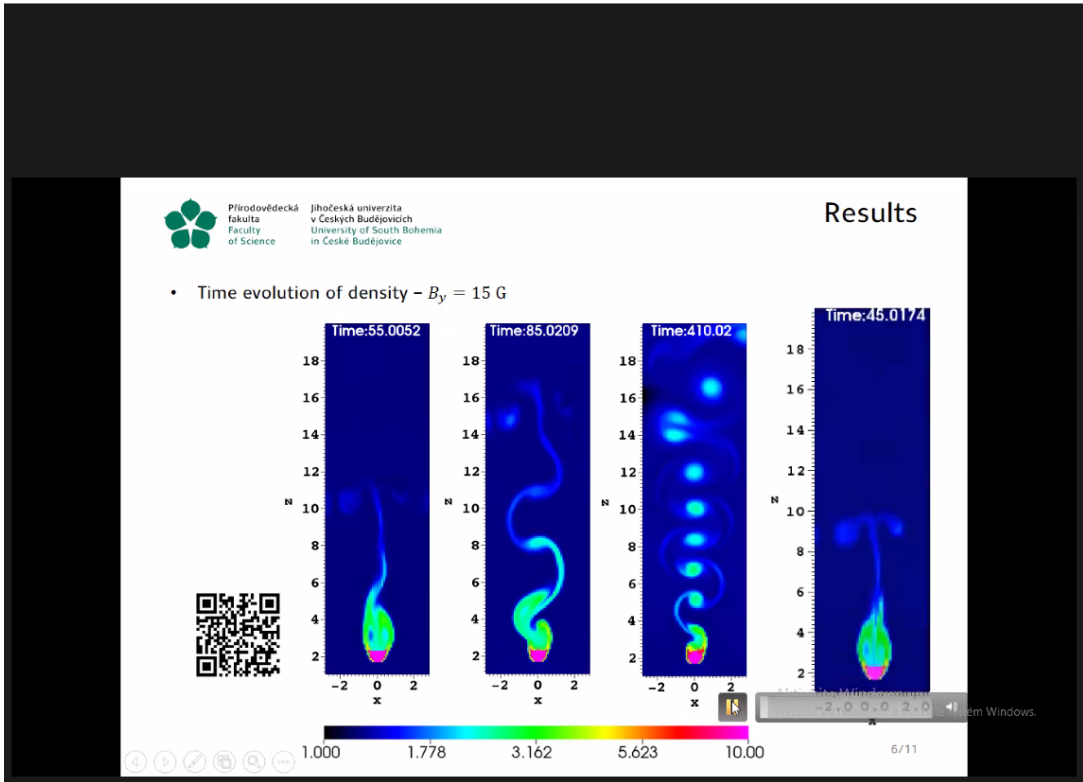

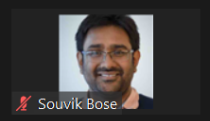
Souvik Bose

Petr Jelínek

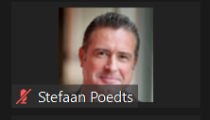
Stefaan Poedts

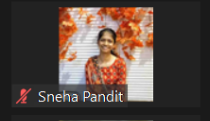
Sneha Pandit

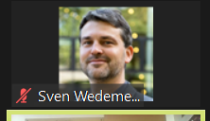
Sven Wedeme...


Sofya Belov

Participants (50)

Find a participant

- PJ Petr Jelínek (Me)
- Souvik Bose (Host)
- SB Sofya Belov (Co-host)
- Sneha Pandit (Co-host)
- Stefaan Poedts (Co-host)
- JS Ejčič, Sonja (Co-host)
- Sowmya Krishnamurthy (Co-host)
- SH Stefan Hofmeister (Co-host)
- GM Galina Motorina
- HP Hardi Peter
- OA Olga Andreeva
- Tom Van Doorsselaere
- YT Yuri Tsap
- Aditi Bhatnagar
- AH Andrew Hillier
- Atul Mohan

Invite Unmute Me

Sem zadejte hledaný výraz

14°C Převáž. oblačno ENG 7:17 07.09.2021